LAWRENCE
LIVERMORE
NATIONAL
LABORATORY

A stable FSI algorithm for light rigid bodies in compressible flow

J. W. Banks, W. D. Henshaw, B. Sjogreen

May 23, 2012

Disclaimer

This document was prepared as an account of work sponsored by an agency of the United States government. Neither the United States government nor Lawrence Livermore National Security, LLC, nor any of their employees makes any warranty, expressed or implied, or assumes any legal liability or responsibility for the accuracy, completeness, or usefulness of any information, apparatus, product, or process disclosed, or represents that its use would not infringe privately owned rights. Reference herein to any specific commercial product, process, or service by trade name, trademark, manufacturer, or otherwise does not necessarily constitute or imply its endorsement, recommendation, or favoring by the United States government or Lawrence Livermore National Security, LLC. The views and opinions of authors expressed herein do not necessarily state or reflect those of the United States government or Lawrence Livermore National Security, LLC, and shall not be used for advertising or product endorsement purposes.

A stable FSI algorithm for light rigid bodies in compressible flow

J. W. Banks[a,1,*], W. D. Henshaw[a,1], B. Sjögreen[a,1]

[a]*Center for Applied Scientific Computing, Lawrence Livermore National Laboratory, Livermore, CA 94551, USA*

Abstract

In this article we describe a stable partitioned algorithm that overcomes the *added mass* instability arising in fluid-structure interaction of light rigid bodies and inviscid compressible flow. The new algorithm is stable even for bodies with zero mass and zero moments of inertia. The approach is based on a local characteristic projection of the force on the rigid body and is a natural extension of the recently developed algorithm for coupling compressible flow and deformable bodies [1, 2, 3]. Normal mode analysis is used to prove the stability of the approximation for a one-dimensional model problem and numerical computations confirm these results. In multiple space dimensions the approach naturally reveals the form of the added mass tensors in the equations governing the motion of the rigid body. These tensors, which depend on certain surface integrals of the fluid impedance, couple the translational and angular velocities of the body. Numerical results in two space dimensions, based on the use of moving overlapping grids and adaptive mesh refinement, demonstrate the behavior and efficacy of the new scheme. These results include the simulation of the difficult problem of a shock impacting an ellipse of zero mass.

Keywords: fluid-structure interaction, added mass instability, moving overlapping grids, compressible fluid flow, rigid bodies

Contents

*Corresponding author. Mailing address: Center for Applied Scientific Computing, L-422, Lawrence Livermore National Laboratory, Livermore, CA 94551, USA. Phone: 925-423-2697. Fax: 925-424-2477.

Email addresses: banks20@llnl.gov (J. W. Banks), henshaw1@llnl.gov (W. D. Henshaw), sjogreen2@llnl.gov (B. Sjögreen)

1. Introduction

The simulation of high-speed compressible fluids interacting with moving bodies is an important class of fluid-structure interaction (FSI) problems. Interesting application areas include understanding the impact of shock or detonation waves on rigid structures and embedded rigid bodies. The numerical simulation of such problems can be difficult, and many techniques have been developed to address various facets of the problem. For a review of FSI see [4] for example. One particularly challenging aspect has been the presence of numerical instabilities that can arise when simulating problems with light bodies. This so-called *added-mass* instability is associated with the fact that the reaction of a body to an applied force depends not only on the mass of the body but also on the fluid displaced by the body through its motion. Traditional partitioned FSI schemes do not take into account the strong coupling between the fluid and solid and thus can exhibit an instability whereby the over-reaction of a light solid to an applied force from the fluid leads in turn to an even larger reaction from the fluid and so on. Fully coupled monolithic approaches to FSI can overcome the unstable behavior but are generally more expensive, can be difficult to implement, and may require advanced solvers or preconditioners. For compressible fluids the instability in partitioned algorithms can often be suppressed by choosing a smaller time-step (as the analysis in this article demonstrates). However, the stable time-step goes to zero as the mass of the body goes to zero and thus alternative approaches to removing the instability are desirable.

In a recent series of articles, we have developed a set of stable interface approximations for partitioned solutions procedures that couple compressible fluids and *deformable* bodies [1, 2, 3]. In [1, 2] the interface approximation is based on a local characteristic analysis that results in an impedance weighted projection of the velocity and forces on the interface. These methods ensure the stability of the partitioned FSI scheme even for *light* solids. In this article we extend these ideas to the coupling of compressible fluids and *rigid bodies*. The key idea presented in this article can be introduced by considering the equations of motion for a rigid body (the full set of equations are presented in full detail in Section 2.2)

$$m_b \dot{\mathbf{v}}_b = \boldsymbol{\mathcal{F}}, \tag{1}$$

$$A\dot{\boldsymbol{\omega}} = -WA\boldsymbol{\omega} + \boldsymbol{\mathcal{T}}, \tag{2}$$

where m_b is the mass of the body, $\mathbf{v}_b(t)$ is the velocity of the center of mass, $\boldsymbol{\omega}(t)$ the angular velocity and A the moment of inertia tensor. $\boldsymbol{\mathcal{F}}$ and $\boldsymbol{\mathcal{T}}$ are, respectively, the force and torque on the body arising from the fluid forces on the surface of the body. From Equations (1)-(2) it would at first seem impossible to solve for $\mathbf{v}_b$ and/or $\boldsymbol{\omega}$ when $m_b = 0$ and/or $A = 0$, as the equations apparently become singular. However, from a local characteristic analysis of the appropriate fluid-structure Riemann problem, we can determine how $\boldsymbol{\mathcal{F}}$ and $\boldsymbol{\mathcal{T}}$ implicitly depend on the motion of the body,

$$\boldsymbol{\mathcal{F}} = -A^{vv}\mathbf{v}_b - A^{v\omega}\boldsymbol{\omega} + \widetilde{\boldsymbol{\mathcal{F}}}, \qquad \boldsymbol{\mathcal{T}} = -A^{\omega v}\mathbf{v}_b - A^{\omega\omega}\boldsymbol{\omega} + \widetilde{\boldsymbol{\mathcal{T}}}. \tag{3}$$

The matrices A^{ij} are the *added-mass* tensors; these are defined in terms of certain integrals of the fluid impedance over the boundary of the rigid body (see Section 6). It is worth pointing out that the concept of added-mass has a long history in describing the motion of embedded bodies in both compressible and incompressible flows. For the compressible regime the recent article [5] nicely discusses the history as well as modern developments.

Using the form of Equation (3) as a starting point, we define a partitioned FSI scheme that remains stable with a large time-step (i.e. the usual time-step restriction associated with the fluid domain in isolation) even as m_b or A go to zero, provided the added-mass tensors satisfy certain properties. This approach relies on the use of an implicit time stepping method for the evolution of the rigid body. The new added-mass scheme is analyzed in detail for a one-dimensional model problem consisting of a rigid body embedded in a fluid governed by the linearized Euler equations. Both a first-order accurate upwind scheme and the second-order accurate Lax-Wendroff scheme are

analyzed using normal mode stability theory [6]. When the rigid body is integrated with an A-stable time-stepping method, the resulting partitioned FSI scheme is shown to be stable with a large time step even when $m_b = 0$.

The added-mass scheme is implemented in two space dimensions using the moving overlapping grid technique described in [7]. In this approach, local body fitted curvilinear grids are used to represent the bodies and these move through static background grids that are often chosen to be Cartesian grids for efficiency. Adaptive mesh refinement (AMR) is used on all grids to dynamically increase resolution locally in space and time. We solve the compressible Euler equations on possibly moving grids in the fluid domain using a high-order extension of Goudnov's method. The Newton-Euler equations (with added-mass corrections) are solved for the motion of the rigid-body using an implicit Runge Kutta scheme (in contrast to the explicit time-stepping method used previously in [7]).

In general, the added-mass scheme proposed here could be used in conjunction with any number of FSI approaches. The treatment of moving geometry is a major component for coupling fluid flow to the motion of rigid bodies and many techniques have been considered. One class of methods relies on a fixed underlying grid and includes, embedded boundaries [8], immersed boundaries [9, 10], level sets [11, 12], and fictitious domain methods [13]. In these methods a body moves through the fixed fluid mesh, and its motion is represented in the fluid as an internal boundary. A second class of methods uses body conforming meshes and allows the mesh to deform in response to the motion of the body. Popular in this class of methods are ALE [14, 15, 16, 17], multiblock [18], and general moving unstructured grids [19].

The remainder of this article is structured as follows. In Section 2, the governing equations of inviscid compressible flow for the fluid, and the Newton-Euler equations for rigid body motion are presented. Section 3 provides some motivation for, and the derivation of, our interface projection scheme in one dimension, showing the origin of the added-mass terms in the equation of motion for the rigid body. In Section 4 this approximation is incorporated into a partitioned FSI scheme for a one-dimensional FSI model problem. The stability of this new added-mass scheme, as well as the traditional coupling scheme, is analyzed using normal mode theory. Section 5 provides numerical confirmation of the theoretical results for the one-dimensional problem, demonstrating the expected convergence rates and stability properties. Extension of the algorithm to multiple space dimensions is presented in Section 6 showing the derivation of added-mass tensors. The time-stepping procedure for the overlapping grid FSI algorithm is summarized in Section 7. Results for two-dimensional problems are presented in Section 8. These include a smoothly receding rigid piston with known solution, a smoothly accelerated ellipse which is compared to the traditional algorithm and a shock-driven zero mass ellipse. The last example is also used to demonstrate the use of adaptive mesh refinement (AMR) and is particularly challenging and interesting. Concluding remarks are given in Section 9. In Appendix A we derive the exact solutions used in the numerical verification of the one-dimensiomal model problem. Finally in Appendix B we present the form of the added mass matrices for a number of simple shapes in two and three-dimensions.

2. Rigid bodies and compressible flow in multiple space dimensions

In this section we define the governing equations for the fluid domains and the rigid bodies. The equations are presented in three space dimensions which serves as a general model. Simplifications to one and two space dimensions, as well as linearization, will be performed later as appropriate.

2.1. The Euler equations for an inviscid compressible fluid

We consider the evolution of a compressible inviscid fluid with an embedded rigid body. The governing equations for the fluid domain $\Omega \subset \mathbb{R}^3$ are the compressible Euler equations

$$\partial_t \mathbf{w} + \nabla \cdot \mathbf{f}(\mathbf{w}) = 0, \qquad \mathbf{x} \in \Omega, \quad t > 0, \tag{4}$$

where $\mathbf{w} = [\rho, \rho\mathbf{v}, \rho\mathcal{E}]^T$ is the vector of conserved variables (density, momentum, energy), $\mathbf{v}$ is the velocity, and $\mathbf{f} = [\rho\mathbf{v}, \rho\mathbf{v} \otimes \mathbf{v} + p\mathbf{I}, (\rho\mathcal{E} + p)\mathbf{v}]^T$ is the flux. The total energy is given by $\rho\mathcal{E} = p/(\gamma - 1) + \frac{1}{2}\rho|\mathbf{v}|^2$ assuming an ideal gas with a constant ratio of specific heats.

2.2. The Newton-Euler equations for the motion of a rigid body

The equations of motion for the rigid body are the Newton-Euler equations which can be written as

$$\dot{\mathbf{x}}_b = \mathbf{v}_b, \tag{5}$$

$$m_b \dot{\mathbf{v}}_b = \boldsymbol{\mathcal{F}}, \tag{6}$$

$$A\dot{\boldsymbol{\omega}} = -WA\boldsymbol{\omega} + \boldsymbol{\mathcal{T}}, \tag{7}$$

$$\dot{E} = WE. \tag{8}$$

Here m_b is the mass of the body, $\mathbf{x}_b(t) \in \mathbb{R}^3$ is the position of the center of mass, and $\mathbf{v}_b(t) \in \mathbb{R}^3$ is the velocity of the center of mass. The moment of inertia matrix $A \in \mathbb{R}^{3 \times 3}$ is defined by

$$A(t) = \int_{B(t)} \rho_b(\mathbf{x})\left[\mathbf{y}^T\mathbf{y}I - \mathbf{y}\mathbf{y}^T\right] d\mathbf{x}, \quad \mathbf{y} = \mathbf{x} - \mathbf{x}_b,$$

where $\rho_b(\mathbf{x})$ defines the mass density of the body and $B(t) \subset \mathbb{R}^3$ defines the region occupied by the body. The inertia matrix is symmetric and positive semi-definite (positive definite if $\rho_b(\mathbf{x}) > 0$) and can be written in terms of the orthogonal matrix $E \in \mathbb{R}^{3\times3}$, whose columns are the principle axes of inertia, $\mathbf{e}_i(t)$, and the diagonal matrix Λ whose diagonal entries are the moments of inertia, I_i,

$$A = E\Lambda E^T, \quad E = [\mathbf{e}_1 \ \mathbf{e}_2 \ \mathbf{e}_3], \quad A\mathbf{e}_i = I_i\mathbf{e}_i, \quad \Lambda = \mathrm{diag}(I_1, I_2, I_3), \quad \mathbf{e}_i^T\mathbf{e}_j = \delta_{ij}.$$

The angular momentum of the body is $\mathbf{h} = A\boldsymbol{\omega}$ where $\boldsymbol{\omega}(t) \in \mathbb{R}^3$ is the angular velocity. The matrix W in (7) is the angular velocity matrix given by

$$W = \mathrm{Cross}(\boldsymbol{\omega}) = \begin{bmatrix} 0 & -\omega_3 & \omega_2 \\ \omega_3 & 0 & -\omega_1 \\ -\omega_2 & \omega_1 & 0 \end{bmatrix}, \quad (\text{ i.e. } W\mathbf{a} = \boldsymbol{\omega} \times \mathbf{a}). \tag{9}$$

The total force and torque on the body are given by

$$\boldsymbol{\mathcal{F}} = \int_{\partial B} \mathbf{f}_s \, ds + \mathbf{f}_b, \quad (\mathbf{f}_s = \text{surface forces}, \mathbf{f}_b = \text{body force}), \tag{10}$$

$$\boldsymbol{\mathcal{T}} = \int_{\partial B} (\mathbf{x} - \mathbf{x}_b) \times \mathbf{f}_s \, ds + \mathbf{g}_b, \quad (\text{torque}), \tag{11}$$

Given $\boldsymbol{\mathcal{F}}(t)$ and $\boldsymbol{\mathcal{T}}(t)$, along with initial conditions, $\mathbf{x}_b(0)$, $\mathbf{v}_b(0)$, $\boldsymbol{\omega}(0)$, and $E(0)$, equations (5)-(8) can be solved to determine $\mathbf{x}_b(t)$, $\mathbf{v}_b(t)$, $\boldsymbol{\omega}(t)$, and $E(t)$ as a function of time.

The motion of a point $\mathbf{r}(t)$ attached to the body is given by a translation together with a rotation about the initial center of mass,

$$\mathbf{r}(t) = \mathbf{x}_b(t) + R(t)(\mathbf{r}(0) - \mathbf{x}_b(0)),$$

where $R(t)$ is the rotation matrix given by

$$R(t) = E(t)E^T(0). \tag{12}$$

The velocity of this point is

$$\dot{\mathbf{r}}(t) = \mathbf{v}_b(t) + WR(t)(\mathbf{r}(0) - \mathbf{x}_b(0)),$$
$$= \mathbf{v}_b(t) + W(\mathbf{r}(t) - \mathbf{x}_b(t)),$$
$$= \mathbf{v}_b(t) + \boldsymbol{\omega} \times (\mathbf{r}(t) - \mathbf{x}_b(t)),$$

Letting $\mathbf{y} = \mathbf{y}(\mathbf{r}) \equiv \mathbf{r}(t) - \mathbf{x}_b(t)$ it follows that the velocity of the point $\mathbf{r}$ can be written in the form

$$\dot{\mathbf{r}}(t) = \mathbf{v}_b(t) - Y\boldsymbol{\omega}, \tag{13}$$

where $Y(t)$ is the matrix

$$Y = \mathrm{Cross}(\mathbf{y}) = \begin{bmatrix} 0 & -y_3 & y_2 \\ y_3 & 0 & -y_1 \\ -y_2 & y_1 & 0 \end{bmatrix}. \tag{14}$$

2.3. The coupling conditions for rigid bodies and inviscid compressible flow

On an interface between a fluid and a solid, the normal component of the fluid velocity must match the normal component of the solid velocity (the inviscid equations allow slip in the tangential direction). Let $\mathbf{r} = \mathbf{r}(t)$ denote a point on the surface of the body B, and $\mathbf{n} = \mathbf{n}(\mathbf{r})$ the outward normal to the body, then

$$\mathbf{n}^T\dot{\mathbf{r}}(t) = \mathbf{n}^T\mathbf{v}(\mathbf{r}(t), t). \tag{15}$$

In addition, the surface force per-unit-area at each point on the body is given by the local force per-unit-area exerted by the fluid,

$$\mathbf{f}_s(\mathbf{r}(t)) = -\mathbf{n}\, p(\mathbf{r}(t), t). \tag{16}$$

3. A partitioned FSI algorithm for the one-dimensional Euler equations and a rigid body – added mass terms

In the recent series of articles [1, 2, 3], a stable interface projection scheme was developed for the problem of coupling a compressible fluid and a deformable elastic solid of arbitrary density. The key result from [1, 2] can be distilled from the consideration of a one-dimensional Riemann problem consisting of a linearized compressible fluid (equations 21) on the right with state (ρ_0, v_0, σ_0), and a linear elastic solid on the left with state $(\bar{\rho}_0, \bar{v}_0, \bar{\sigma}_0)$. Arguments based on characteristics were used to show that for positive times the interface values (v_I, σ_I) are given in terms of an impedance weighted average of the fluid and solid states,

$$v_I = \frac{\bar{z}\bar{v}_0 + z v_0}{\bar{z} + z} + \frac{\sigma_0 - \bar{\sigma}_0}{\bar{z} + z}, \tag{17}$$

$$\sigma_I = \frac{\bar{z}^{-1}\bar{\sigma}_0 + z^{-1}\sigma_0}{\bar{z}^{-1} + z^{-1}} + \frac{v_0 - \bar{v}_0}{\bar{z}^{-1} + z^{-1}}. \tag{18}$$

Here $\bar{z} = \bar{\rho}c_p$ is the solid impedance based on the speed of sound, c_p, for compression waves in the solid, while $z = \rho c$ is the fluid impedance based on the speed of sound, c, in the fluid. In [1, 2] it was found that using a projection to impose (17) and (18) as interface conditions resulted in a scheme that remained stable, even in the presence of *light* solids when the traditional FSI coupling scheme fails.   See [1, 2, 3] for further details.

The present situation of a rigid body can be considered through a limit process where c_p becomes large compared to c, and the elastic body becomes increasingly rigid. Taking the formal limit $\bar{z}/z \to \infty$ in equations (17)-(18), with z fixed, results in[2]

$$v_I = \bar{v}_0, \tag{19}$$

$$\sigma_I = \sigma_0 + z(v_0 - \bar{v}_0). \tag{20}$$

Thus for a rigid body, the interface surface stress is equal to the stress from the fluid plus z times the difference of the fluid velocity and the velocity of the body. The dependence of the interface stress, σ_I, on the velocity of the body, $\bar{v}_0$, has thus been exposed.

These interface conditions can be derived more directly by considering the *Riemann-like* problem, shown in Fig. 1, that consists of a rigid body of mass m_b adjacent to a compressible fluid governed by the linearized Euler equations. Using characteristic theory, we can write an explicit equation for the motion for the rigid body in terms of the initial conditions. This process introduces an added mass term into the equations, and the motion of the body is seen to be well defined even when $m_b = 0$. The equations are then written in an alternative form as an interface projection that is localized in space and time. This form can be used to generalize the approach to multiple dimensions.

Consider then the solution to the linearized one-dimensional Euler equations for an inviscid compressible fluid, in the moving domain $x > r_b(t)$ as shown in Fig. 1,

$$\begin{cases} \partial_t \rho + \hat{v}\partial_x \rho + \hat{\rho}\partial_x v = 0 \\ \partial_t v + \hat{v}\partial_x v - (1/\hat{\rho})\partial_x \sigma = 0 \ , \quad \text{for } x > r_b(t), \\ \partial_t \sigma + \hat{v}\partial_x \sigma - \hat{\rho}\hat{c}^2 \partial_x v = 0 \end{cases} \tag{21}$$

$$[\rho(x,0), v(x,0), \sigma(x,0)] = [\rho_0(x), v_0(x), \sigma_0(x)]. \tag{22}$$

Here $\sigma = -p$ is the fluid stress. The equations have been linearized about the constant state $[\hat{\rho}, \hat{v}, \hat{p}]$. The linearized speed of sound is $\hat{c} = \sqrt{\gamma\hat{p}/\hat{\rho}}$ and the the initial conditions are given by $[\rho_0(x), v_0(x), \sigma_0(x)]$. The fluid is coupled to a rigid body of mass m_b whose motion is governed by Newton's law of motion for the velocity, v_b, and the position, x_b, of the center of mass,

$$m_b \dot{v}_b = \sigma(r_b(t), t)\mathcal{A}_b + f_b, \tag{23}$$

$$\dot{x}_b = v_b. \tag{24}$$

Here $\mathcal{A}_b$ is the cross-sectional area of the body, f_b is an external body force and $r_b = x_b + w_b/2$ defines the point on the body that lies next to the fluid (w_b being the constant width of the body).

From the theory of characteristics, the characteristic variable $\chi = \sigma + zv$ is constant along the C^- characteristic $dx/dt = -s = \hat{v} - \hat{c}$. Therefore, for a point $r_b(t)$ on the body, $\chi(r_b, t) = \chi(r_b + st, 0)$, and thus

$$\sigma(r_b, t) + zv(r_b, t) = \sigma_0(r_b + st) + zv_0(r_b + st). \tag{25}$$

Using the interface condition $v(r_b, t) = v_b(t)$ it follows that the stress on the body is

$$\sigma(r_b, t) = \sigma_0(r_b + st) + z\big(v_0(r_b + st) - v_b\big). \tag{26}$$

---

[2]This limit process could be quite complex and we are speaking here on informal grounds for motivational purposes.
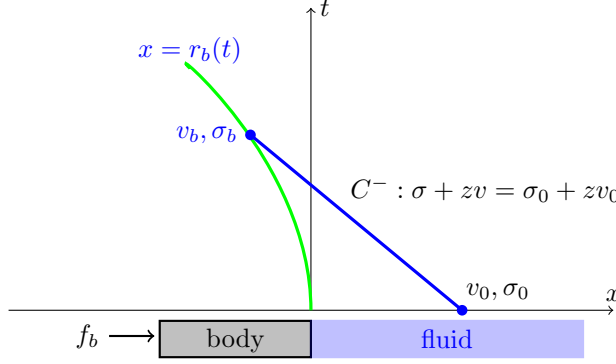
Figure 1: The x-t diagram for the one-dimensional fluid/rigid-body problem.

Substituting (26) into (23) gives an equation for the motion of the body that only depends on the initial data in the fluid and the external body force,

$$m_b \dot{v}_b = \sigma_0(r_b + st)\mathcal{A}_b + z\mathcal{A}_b\big(v_0(r_b + st) - v_b\big) + f_b(t), \tag{27}$$

$$\dot{r}_b = v_b. \tag{28}$$

This equation can be written in the form,

$$m_b \dot{v}_b + z\mathcal{A}_b v_b = \sigma_0(r_b + st)\mathcal{A}_b + z\mathcal{A}_b v_0(r_b + st) + f_b(t), \tag{29}$$

$$\dot{r}_b = v_b, \tag{30}$$

where the *added mass term* $z\mathcal{A}_b v_b$ has been moved to the left-hand side. Note that equations (29)-(30) can be used to solve for v_b *even when* $m_b = 0$ (provided $z\mathcal{A}_b > 0$). By using an ODE integration scheme that treats the added mass term $z\mathcal{A}_b v_b$ implicitly, equation (29) can be used to evolve the rigid body with a time step that need not go to zero as m_b goes to zero. In practical implementation, it is often beneficial to localize (26) in space and time. Using $\chi(t) = \chi(t - \epsilon)$ along the C^- characteristic and letting $\epsilon \to 0$ leads to the relation

$$\sigma(r_b, t) = \sigma(r_b+, t-) + z\big(v(r_b+, t-) - v_b(t)\big). \tag{31}$$

Here $\sigma(r_b+, t-)$ and $v(r_b+, t-)$ denote the stress and velocity in the fluid at a point which lies an infinitesimal distance backward along the C^- characteristic. Equation (31) is in a form that can be used in an interface projection strategy and can be easily generalized to a multidimensional problem as is done in Section 6. Furthermore, notice the similarity of (31) to equation (20). This hints at the close connection between (31) and the projection schemes evaluated in [1, 2, 3] for coupling compressible fluids and deformable bodies.

4. Normal mode stability analysis of idealized model problem

In order to understand the stability of a numerical scheme that uses the new interface conditions (31), consider the one-dimensional model problem of a rigid body confined on either side by an inviscid compressible fluid, as shown in Fig.2. As in [1] we can linearize and freeze coefficients about a reference state to arrive at a problem where the equations of acoustics govern the two fluids, and Newtonian mechanics govern the motion of the solid. As shown in Fig. 2, the body has a width of w_b and its cross-sectional area is assumed to be 1. Note that the equations for the fluids are defined in fixed reference coordinates, $x < -w_b/2$ and $x > w_b/2$.

More specifically, the governing equations for the fluid in the left domain are given by

$$\begin{bmatrix} v_L \\ \sigma_L \end{bmatrix}_t - \begin{bmatrix} 0 & \frac{1}{\rho_L} \\ \rho_L c_L^2 & 0 \end{bmatrix} \begin{bmatrix} v_L \\ \sigma_L \end{bmatrix}_x = 0, \quad \text{for} \quad x < -\frac{w_b}{2}, \tag{32}$$

while those for the fluid in the right domain are

$$\begin{bmatrix} v_R \\ \sigma_R \end{bmatrix}_t - \begin{bmatrix} 0 & \frac{1}{\rho_R} \\ \rho_R c_R^2 & 0 \end{bmatrix} \begin{bmatrix} v_R \\ \sigma_R \end{bmatrix}_x = 0, \quad \text{for} \quad x > \frac{w_b}{2}. \tag{33}$$

The motion of the rigid body is governed by

$$m_b \dot{v}_b = \mathcal{F}, \tag{34}$$

where the force exerted on the rigid body by the fluid is

$$\mathcal{F} = \sigma_R|_{x=w_b/2} - \sigma_L|_{x=-w_b/2}. \tag{35}$$
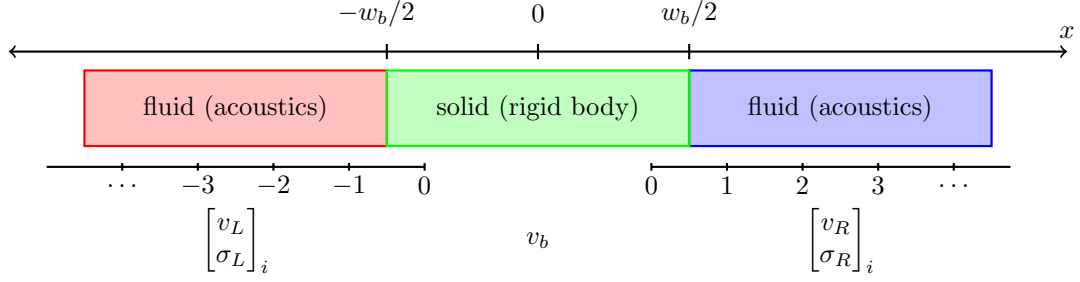
6

Figure 2: Schematic of the one-dimensional FSI model problem used in the stability analysis. A solid rigid body is embedded between a fluid domain on the left and a fluid domain on the right. The boundaries of the rigid body are located mid-way between the ghost points of the fluid grids with index $i = 0$ and the first grid point inside the domain with index $i = -1$ on the left and $i = 1$ on the right.

The system is closed using interface conditions at $x = \pm w_b/2$ which enforce continuity of velocity, namely

$$v_L|_{x=-w_b/2} = v_b \tag{36}$$

$$v_R|_{x=w_b/2} = v_b. \tag{37}$$

Notice that the problem is posed in a moving reference frame (which we call x), and the frame attached to the rigid body can be calculated as

$$\hat{x} = x + \int_0^t v_b(\tau) \, d\tau.$$

4.1. A first-order accurate numerical discretization of the model problem

This section describes the discretization of the governing equations (32)-(34) to first-order accuracy. As in [1], Godunov style upwind schemes will be used to discretize the fluid domains. We will analyze and demonstrate the properties of these schemes when combined with various discrete interface conditions. The finite difference grid for the discretization of the one-dimensional problem is outlined in Fig. 2. Note that the left and right boundaries of the rigid body are located at the mid-point of computational cells. This choice is made for notational convenience, but is not critical to the analysis. The grid points to the left of the rigid body are denoted by

$$x_{L,i} = -\frac{w_b}{2} + \left(i + \frac{1}{2}\right)\Delta x_L, \quad i = \ldots, -2, -1, 0,$$

and to the right by

$$x_{R,i} = \frac{w_b}{2} + \left(i - \frac{1}{2}\right)\Delta x_R, \quad i = 0, 1, 2, \ldots.$$

Ghost points, corresponding to index $i = 0$ for both domains, will be used to enforce the interface conditions.

Let $z_k = \rho_k c_k$ denote the acoustic impedance in domain $k = L, R$. The eigen-decomposition of the matrices in (32) and (33) is given by

$$C_k \equiv \begin{bmatrix} 0 & \frac{1}{\rho_k} \\ \rho_k c_k^2 & 0 \end{bmatrix} = R_k \Lambda_k R_k^{-1}, \quad R_k = c_k \begin{bmatrix} -1 & 1 \\ z_k & z_k \end{bmatrix}, \quad \Lambda_k = \begin{bmatrix} -c_k & 0 \\ 0 & c_k \end{bmatrix}, \quad R_k^{-1} = \frac{1}{2 c_k z_k} \begin{bmatrix} -z_k & 1 \\ z_k & 1 \end{bmatrix}. \tag{38}$$

Let $v_{k,i}^n \approx v_k(x_{k,i}, t^n)$ and $\sigma_{k,i}^n \approx \sigma_k(x_{k,i}, t^n)$ denote discrete approximations to the velocity and stress at time $t^n = n\Delta t$. We also use the notation

$$\begin{bmatrix} v_k \\ \sigma_k \end{bmatrix}_i^n \equiv \begin{bmatrix} v_{k,i}^n \\ \sigma_{k,i}^n \end{bmatrix}.$$

The first-order accurate upwind scheme is given by

$$\begin{bmatrix} v_k \\ \sigma_k \end{bmatrix}_i^{n+1} = \begin{bmatrix} v_k \\ \sigma_k \end{bmatrix}_i^n + \Delta t R_k \Lambda_k^- R_k^{-1} D_- \begin{bmatrix} v_k \\ \sigma_k \end{bmatrix}_i^n + \Delta t R_k \Lambda_k^+ R_k^{-1} D_+ \begin{bmatrix} v_k \\ \sigma_k \end{bmatrix}_i^n, \tag{39}$$

for $i = \ldots, -2, -1$ on the left and for $i = 1, 2 \ldots$ on the right. The negative and positive parts of the wave speeds are defined by

$$\Lambda_k^- = \begin{bmatrix} -c_k & 0 \\ 0 & 0 \end{bmatrix} \quad \text{and} \quad \Lambda_k^+ = \begin{bmatrix} 0 & 0 \\ 0 & c_k \end{bmatrix}, \tag{40}$$

respectively. The forward and backward divided differences are defined by $D_+ u_i = (u_{i+1} - u_i)/\Delta x$ and $D_- u_i = D_+ u_{i-1}$, where Δx is taken for the appropriate domain.

7

The methods we consider can be presented using a unified notation. Motivated by the discussion in Section 3, the interface stresses at t^{n+1} for the first-order scheme are defined by

$$\sigma_{I,L}^{n+1} = \sigma_{L,-1}^{n+1} + \alpha_L \left(v_b^{n+1} - v_{L,-1}^{n+1} \right) \tag{41}$$

$$\sigma_{I,R}^{n+1} = \sigma_{R,1}^{n+1} + \alpha_R \left(v_{R,1}^{n+1} - v_b^{n+1} \right). \tag{42}$$

where α_L and α_R are parameters that can be used to obtain various discrete interface conditions. The traditional approach found in the literature can be described in words as applying the velocity from the solid as a boundary condition on the fluids, and applying the stress in the fluid to derive the applied force on the body. This condition is achieved by setting $\alpha_k = 0$. Our new projection interface condition is given by setting $\alpha_k = z_k$.

The solution state in the ghost cells at t^{n+1} is defined to first-order accuracy by imposing continuity of the velocity at the interfaces

$$v_{L,0}^{n+1} = v_b^{n+1}, \tag{43}$$

$$v_{R,0}^{n+1} = v_b^{n+1}, \tag{44}$$

and extrapolation of the stress to first-order accuracy as

$$\sigma_{L,0}^{n+1} = \sigma_{I,L}^{n+1}, \tag{45}$$

$$\sigma_{R,0}^{n+1} = \sigma_{I,R}^{n+1}. \tag{46}$$

The rigid body equations (34) are advanced in time with the backward Euler scheme,

$$m_b v_b^{n+1} = m_b v_b^n + \Delta t \mathcal{F}^{n+1} \tag{47}$$

where the force at t^{n+1}, $\mathcal{F}^{n+1}$, is defined as

$$\mathcal{F}^{n+1} = \sigma_{I,R}^{n+1} - \sigma_{I,L}^{n+1}. \tag{48}$$

The backward Euler method is used here in order to simplify the analysis. Used in isolation, the backward-Euler scheme is unconditionally stable for any Δt independent of m_b provided $m_b > 0$. We will show, however, that the fully coupled FSI problem has a time-step restriction that depends on m_b for the *traditional* interface coupling scheme. For the new interface projection scheme we show that there is no dependence of the stable time step on m_b. The backward-Euler scheme is, of course, only first-order accurate. For higher-order accuracy one can use implicit Runge-Kutta schemes, as described in Section 7 where we extend the scheme to multiple space dimensions. Note that while implicit schemes may be more expensive per time-step than an explicit schemes, they are only used to solve the rigid body equations which consist of just a few ODEs. As an alternative to implicit schemes, one can consider using an explicit scheme with a sub-cycling approach (i.e. taking multiple sub-steps with a smaller value for Δt). Some remarks on these issues will be provided where appropriate.

In summary, to advance one time level from t^n to t^{n+1} using the first-order accurate scheme, the following steps can be followed

Algorithm 1.

1. *Compute* $\begin{bmatrix} v_L \\ \sigma_L \end{bmatrix}_i^{n+1}$ *for* $i = \dots, -2, -1$ *and* $\begin{bmatrix} v_R \\ \sigma_R \end{bmatrix}_i^{n+1}$ *for* $i = 1, 2, \dots$ *by (39).*
2. *Set* $\mathcal{F}^{n+1} = \sigma_{R,1}^{n+1} + \alpha_R(v_{R,1}^{n+1} - v_b^{n+1}) - \sigma_{L,-1}^{n+1} - \alpha_L(v_b^{n+1} - v_{L,-1}^{n+1})$, *and solve (47) for* v_b^{n+1},

$$v_b^{n+1} = \left[m_b + \Delta t(\alpha_L + \alpha_R) \right]^{-1} \left[m_b v_b^n + \Delta t \left(\sigma_{R,1}^{n+1} + \alpha_R v_{R,1}^{n+1} - (\sigma_{L,-1}^{n+1} - \alpha_L v_{L,-1}^{n+1}) \right) \right]. \tag{49}$$

3. *Define the ghost point values by the velocity boundary conditions (43) and (44), along with the stress extrapolations (45) and (46).*

4.2. Normal mode analysis of the first-order scheme

Next, we analyze the stability of the interface discretizations, and investigate how the choice of α_L and α_R affect the behavior of the overall numerical method. To simplify the presentation, assume $c_L = c_R = c$, $\rho_L = \rho_R = \rho$, $\Delta x_L = \Delta x_R = \Delta x$, and $\alpha_L = \alpha_R = \alpha$. In addition set $z = z_L = z_R$. These assumptions are purely for convenience and clarity, and do not materially change the results of the analysis. We pursue a stability analysis via the normal mode theory of Gustafsson Kreiss and Sundström (GKS) [6].

As was done in [1], we seek normal mode solutions of the form

$$\begin{bmatrix} v_k \\ \sigma_k \end{bmatrix}_i^n = \mathcal{A}^n \begin{bmatrix} \tilde{v}_k \\ \tilde{\sigma}_k \end{bmatrix}_i, \qquad v_b^n = \mathcal{A}^n \tilde{v}_b, \qquad \text{for } k = L, R, \tag{50}$$

8

where $\tilde{v}_{k,i}$ and $\tilde{\sigma}_{k,i}$ are bounded functions of space, and $\mathcal{A}$, the amplification factor, is a complex scalar with $|\mathcal{A}| > 1$. If such a non-zero solution can be found, the approximation grows unboundedly in time. Conversely, if no such solutions exist for $\mathcal{A} \geq 1$, (with the limit case $\mathcal{A} = 1$ treated as the limit from $\mathcal{A} > 1$) then the scheme is stable. Characteristic normal modes are denoted by

$$\begin{bmatrix} a_k \\ b_k \end{bmatrix}_i = R_k^{-1} \begin{bmatrix} \tilde{v}_k \\ \tilde{\sigma}_k \end{bmatrix}_i = \frac{1}{2cz} \begin{bmatrix} \tilde{\sigma}_k - z\tilde{v}_k \\ \tilde{\sigma}_k + z\tilde{v}_k \end{bmatrix}_i. \tag{51}$$

Insertion of (50) into the finite difference scheme (39) leads to

$$\left.\begin{aligned} \mathcal{A}a_{L,i} &= a_{L,i} - \lambda\left(a_{L,i} - a_{L,i-1}\right) \\ \mathcal{A}b_{L,i} &= b_{L,i} + \lambda\left(b_{L,i+1} - b_{L,i}\right) \end{aligned}\right\} \qquad \text{for } i = \ldots, -3, -2, -1 \tag{52}$$

and

$$\left.\begin{aligned} \mathcal{A}a_{R,i} &= a_{R,i} - \lambda\left(a_{R,i} - a_{R,i-1}\right) \\ \mathcal{A}b_{R,i} &= b_{R,i} + \lambda\left(b_{R,i+1} - b_{R,i}\right) \end{aligned}\right\} \qquad \text{for } i = 1, 2, 3, \ldots \tag{53}$$

where $0 < \lambda = c\Delta t/\Delta x < 1$. Define the quantity

$$r = \frac{\mathcal{A} - 1 + \lambda}{\lambda}.$$

We see that $|r| > 1$ by rewriting $|r|^2 > 1$ in terms of the polar variables R and θ, where $\mathcal{A} = Re^{i\theta}$. By simple algebraic manipulations, $|r|^2 > 1$ can be rewritten as

$$(R - 1)^2 + 2\lambda(R - 1) + 2R(1 - \lambda)(1 - \cos\theta) > 0,$$

which is true since $R > 1$ and $\lambda < 1$.

For the two components on characteristics coming in from infinity, the solution to the difference equations (52) and (53) is

$$a_{L,i} = r^{-(i+1)} a_{L,-1}, \qquad \text{for } i = \ldots, -3, -2, -1,$$

$$b_{R,i} = r^{(i-1)} b_{R,1}, \qquad \text{for } i = 1, 2, 3, \ldots.$$

The assumption of boundedness as $i \to \pm\infty$ gives $a_{L,i} = 0$ for $i \ldots, -3, -2, -1$, and $b_{R,i} = 0$ for $i = 1, 2, 3, \ldots$. Note that $a_{L,0}$ and $b_{R,0}$ do not play a role in the difference equations (52) and (53), but their values can be determined algebraically using the interface conditions

$$a_{L,0} = \frac{\alpha - z}{2z}(\tilde{v}_b/c - b_{L,-1}),$$

$$b_{R,0} = \frac{z - \alpha}{2z}(\tilde{v}_b/c + a_{R,1}).$$

The remainder of the solution to difference equations (52) and (53) is given by

$$a_{R,i} = r^{-i} a_{R,0}, \qquad \text{for } i = 0, 1, 2, 3, \ldots, \tag{54}$$

$$b_{L,i} = r^{i} b_{L,0}, \qquad \text{for } i = \ldots, -3, -2, -1, 0. \tag{55}$$

The solutions (54) and (55) are bounded because $|r| > 1$. The definition of the characteristic normal modes on the interior yields

$$\begin{bmatrix} \tilde{v} \\ \tilde{\sigma} \end{bmatrix}_{L,i} = c \begin{bmatrix} 1 \\ z \end{bmatrix} r^{i} b_{L,0} \qquad \text{for } i = \ldots, -3, -2, -1 \tag{56}$$

and

$$\begin{bmatrix} \tilde{v} \\ \tilde{\sigma} \end{bmatrix}_{R,i} = c \begin{bmatrix} -1 \\ z \end{bmatrix} r^{-i} a_{R,0} \qquad \text{for } i = 1, 2, 3, \ldots. \tag{57}$$

The three undetermined constants $b_{L,0}$, $a_{R,0}$, and $\tilde{v}_b$ are defined by application of the interface conditions (43)-(46) and the rigid body integrator (47). This leads to the linear system of equations

$$\begin{bmatrix} 1 + \dfrac{\alpha - z}{2zr} & 0 & -\dfrac{\alpha + z}{2z} \\[2ex] 0 & 1 + \dfrac{\alpha - z}{2zr} & \dfrac{\alpha + z}{2z} \\[2ex] \dfrac{\mathcal{A}\Delta t}{r}(z - \alpha) & -\dfrac{\mathcal{A}\Delta t}{r}(z - \alpha) & m_b(\mathcal{A} - 1) + 2\Delta t\alpha\mathcal{A} \end{bmatrix} \begin{bmatrix} b_{L,0} \\ a_{R,0} \\ \tilde{v}_b/c \end{bmatrix} = 0. \tag{58}$$

The system (58) is an eigenvalue problem for $\mathcal{A}$, in the sense that if there is an $\mathcal{A}$ such that the determinant of the system is zero, then there exists a non-trivial solution of the form (50). If, furthermore, $|\mathcal{A}| > 1$, then the solution (50) grows in time.

Theorem 1. *The numerical scheme using the interior discretizations (39), interface conditions (43)-(46), rigid body integrator (47) and projections (41)-(42) with $\alpha = z$ has no eigenvalues $\mathcal{A}$ with $|\mathcal{A}| > 1$ for $\lambda \leq 1$ and $m_b \geq 0$.*

Proof. For $\alpha = z$ the eigenvalue problem (58) reduces to

$$
\begin{bmatrix}
1 & 0 & -1 \\
0 & 1 & 1 \\
0 & 0 & m_b(\mathcal{A} - 1) + 2\Delta t z \mathcal{A}
\end{bmatrix}
\begin{bmatrix}
b_{L,0} \\
a_{R,0} \\
\tilde{v}_b / c
\end{bmatrix} = 0.
\tag{59}
$$

The determinant is zero when $\mathcal{A} = m_b/(m_b + 2\Delta t z)$. By assumption, $\Delta t > 0$ and $z > 0$ and so $|\mathcal{A}| < 1$. $\qquad\square$

Theorem 2. *The numerical scheme using the interior discretizations (39), interface conditions (43)-(46), rigid body integrator (47) and projections (41)-(42) with $\alpha = 0$ has no eigenvalues $\mathcal{A}$ with $|\mathcal{A}| > 1$ when*

$$
\Delta t < m_b(4 - \lambda)/(z\lambda)
\tag{60}
$$

for $\lambda \leq 1$. Conversely, if $\Delta t > m_b(4 - \lambda)/(z\lambda)$, then there are eigenvalues with $|\mathcal{A}| > 1$ for $\lambda \leq 1$.

Proof. For $\alpha = 0$, the eigenvalue problem (58) reduces to

$$
\begin{bmatrix}
1 - \dfrac{1}{2r} & 0 & -\dfrac{1}{2} \\[2mm]
0 & 1 - \dfrac{1}{2r} & \dfrac{1}{2} \\[2mm]
\dfrac{\mathcal{A}z\Delta t}{r} & -\dfrac{\mathcal{A}z\Delta t}{r} & m_b(A - 1)
\end{bmatrix}
\begin{bmatrix}
b_{L,0} \\
a_{R,0} \\
\tilde{v}_b / c
\end{bmatrix} = 0.
\tag{61}
$$

The zero determinant condition is solved to give three roots $\mathcal{A}_1 = 1 - \lambda/2$ and

$$
\mathcal{A}_{2,3} = 1 - \frac{\lambda}{4} - \frac{z\xi\lambda}{2} \pm \sqrt{\left(1 - \frac{\lambda}{4} - \frac{z\xi\lambda}{2}\right)^2 - 1 + \frac{\lambda}{2}}
\tag{62}
$$

where $\xi = \Delta t / m_b$. Clearly, $|\mathcal{A}_1| < 1$ for $\lambda \leq 1$. In the case

$$
\left(1 - \frac{\lambda}{4} - \frac{z\xi\lambda}{2}\right)^2 - 1 + \frac{\lambda}{2} < 0,
$$

$\mathcal{A}_2$ and $\mathcal{A}_3$ are complex conjugate, and

$$
|\mathcal{A}_2|^2 = |\mathcal{A}_3|^2 = \left(1 - \frac{\lambda}{4} - \frac{z\xi\lambda}{2}\right)^2 - \left(1 - \frac{\lambda}{4} - \frac{z\xi\lambda}{2}\right)^2 + 1 - \frac{\lambda}{2} = 1 - \frac{\lambda}{2} < 1.
$$

When $\mathcal{A}_2$ and $\mathcal{A}_3$ are real, rewriting (62) as

$$
A_{2,3} = 1 - \left(\frac{\lambda}{4} + \frac{z\xi\lambda}{2}\right) \pm \sqrt{\left(\frac{\lambda}{4} + \frac{z\xi\lambda}{2}\right)^2 - z\xi\lambda}
$$

shows directly that both roots are are always < 1, hence $|\mathcal{A}| < 1$ if and only if

$$
-1 < 1 - \left(\frac{\lambda}{4} + \frac{z\xi\lambda}{2}\right) - \sqrt{\left(\frac{\lambda}{4} + \frac{z\xi\lambda}{2}\right)^2 - z\xi\lambda}
$$

which is equivalent to

$$
\sqrt{\left(\frac{\lambda}{4} + \frac{z\xi\lambda}{2}\right)^2 - z\xi\lambda} < 2 - \left(\frac{\lambda}{4} + \frac{z\xi\lambda}{2}\right).
\tag{63}
$$

The necessary condition that the right hand side is positive is equivalent to

$$
z\xi\lambda < 4 - \frac{\lambda}{2}.
\tag{64}
$$

Assume (64) holds and square both sides of (63) to obtain

$$
z\xi\lambda < 4 - \lambda.
\tag{65}
$$

Hence, $|\mathcal{A}| < 1$ exactly when (65) holds. The proof is completed by observing that (65) is equivalent to (60). $\qquad\square$

Remark: Theorem 2 means that an explicit ODE type of time step restriction exists for the coupled problem, even though (34) is integrated by an unconditionally stable ODE integrator. In the case of light bodies, i.e., bodies with small m_b, this time step restriction can be severe. Another way to state the result is that for any fixed grid resolution, there exists some sufficiently small mass that the scheme will give a solution that grows exponentially in time. In fact, it is easy to see that for $\alpha = 0$ and fixed Δt, the limit of small mass yields $r \sim 1 - \lambda/4 - z\lambda\Delta t/m_b$ and therefore $\lim_{m_b \to 0} |\mathcal{A}| = \infty$. Note however, that for finite mass the method with $\alpha = 0$ is formally stable in the sense of PDE stability, since the eigenvalues will eventually be smaller than one when Δx and $\Delta t \to 0$, for fixed λ.

Remark: Theorem 1 shows that the time step restriction (60) is easy to avoid by switching to the interface conditions with $\alpha = z$.

Remark: The structure of the eigenvalue problem in the proof of Theorem 1 shows why the choice $\alpha = z$ is in some sense optimal. When $\alpha = z$, the evolution of the rigid body equation is decoupled from the evolution of two fluid domains and stability for any nonnegative rigid body mass is obtained. This is the primary implication of Theorem 1. On the other hand, for $\alpha = 0$, the eigenvalue problem (58) represents a coupled system and the question of stability is summarized in Theorem 2.

Remark: For choices of α other than zero or z, the stability of the numerical scheme varies somewhat. The determinant condition can be used to produce an expression for $\mathcal{A}$, but it is somewhat difficult to interpret. We provide no further discussion about other choices of the parameter α.

4.3. A second-order accurate numerical discretization of the model problem

We look now at the formulation and stability of a second-order version of the projection interface scheme. For the discretization of the fluid domains we choose the second-order accurate Lax-Wendroff scheme,

$$\begin{bmatrix} v_k \\ \sigma_k \end{bmatrix}_i^{n+1} = \begin{bmatrix} v_k \\ \sigma_k \end{bmatrix}_i^n + \Delta t C_k D_0 \begin{bmatrix} v_k \\ \sigma_k \end{bmatrix}_i^n + \frac{\Delta t^2}{2} C_k^2 D_+ D_- \begin{bmatrix} v_k \\ \sigma_k \end{bmatrix}_i^n \qquad k = L, R \tag{66}$$

where $D_0 = (D_+ + D_-)/2$ is the centered difference operator, and C_k has been defined previously in (38). The Lax-Wendroff scheme is a good model, since many non-linear schemes of TVD type are designed to approximate the Lax-Wendroff scheme in the parts of the computational domain where the solution is smooth. The projection coupling conditions can be implemented to second-order accuracy as follows. Define interface stresses on the left and right at any time t^n by

$$\sigma_{I,L}^n = \frac{3\sigma_{L,-1}^n - \sigma_{L,-2}^n}{2} + \alpha_L \left(v_b^n - \frac{3v_{L,-1}^n - v_{L,-2}^n}{2} \right) \tag{67}$$

$$\sigma_{I,R}^n = \frac{3\sigma_{R,1}^n - \sigma_{R,2}^n}{2} + \alpha_R \left(\frac{3v_{R,1}^n - v_{R,2}^n}{2} - v_b^n \right). \tag{68}$$

These are obtained by extrapolation from domain interiors, and subsequent projection. The force at any time level t^n is defined as before using (48), and a second-order accurate trapezoidal integration for the solid is then defined

$$m_b \frac{v_b^{n+1} - v_b^n}{\Delta t} = \frac{1}{2} \left(\mathcal{F}^{n+1} + \mathcal{F}^n \right). \tag{69}$$

The velocity from the solid is applied as a boundary condition on the fluids to second-order accuracy by setting the average $(v_{L,0} + v_{L,-1})/2$ equal to v_b (and similarly at the right interface), or equivalently

$$v_{L,0}^n = 2v_b^n - v_{L,-1}^n \tag{70}$$

$$v_{R,0}^n = 2v_b^n - v_{R,1}^n. \tag{71}$$

Extrapolation of the stress to the ghost cells gives

$$\sigma_{L,0}^n = 2\sigma_{I,L}^n - \sigma_{L,-1}^n \tag{72}$$

$$\sigma_{R,0}^n = 2\sigma_{I,R}^n - \sigma_{R,1}^n. \tag{73}$$

In summary, to advance one time level from t^n to t^{n+1} using the second-order accurate scheme, the following steps can be followed

Algorithm 2.

1. *Compute* $\begin{bmatrix} v_L \\ \sigma_L \end{bmatrix}_i^{n+1}$ *for* $i = \ldots, -2, -1$ *and* $\begin{bmatrix} v_R \\ \sigma_R \end{bmatrix}_i^{n+1}$ *for* $i = 1, 2, \ldots$ *using (66).*

2. *Define F^{n+1} using the computed solution at t^{n+1} and solve (69) to yield*

$$v_b^{n+1} = \left[m_b + \frac{\Delta t \alpha_L}{2} + \frac{\Delta t \alpha_R}{2} \right]^{-1} \left[\left(m_b - \frac{\Delta t \alpha_L}{2} - \frac{\Delta t \alpha_R}{2} \right) v_b^n + \right.$$

$$\frac{\Delta t}{2} \left(\frac{3\sigma_{R,1}^{n+1} - \sigma_{R,2}^{n+1}}{2} + \frac{3\sigma_{R,1}^n - \sigma_{R,2}^n}{2} \right) - \frac{\Delta t}{2} \left(\frac{3\sigma_{L,-1}^{n+1} - \sigma_{L,-2}^{n+1}}{2} + \frac{3\sigma_{L,-1}^n - \sigma_{L,-2}^n}{2} \right) +$$

$$\left. \frac{\alpha_R \Delta t}{2} \left(\frac{3v_{R,1}^{n+1} - v_{R,2}^{n+1}}{2} + \frac{3v_{R,1}^n - v_{R,2}^n}{2} \right) + \frac{\alpha_L \Delta t}{2} \left(\frac{3v_{L,-1}^{n+1} - v_{L,-2}^{n+1}}{2} + \frac{3v_{L,-1}^n - v_{L,-2}^n}{2} \right) \right]. \tag{74}$$

3. *Define the ghost point values for the fluid domains using (70) – (73).*

4.4. Normal mode analysis of the second-order scheme

For the analysis, we make the same assumptions as in Sec. 4.2, that the grid spacings and wave speeds are the same on both sides of the body and that $\alpha_L = \alpha_R = \alpha$. First, we decompose (66) into characteristic components, and obtain the two scalar equations on each side of the body,

$$a_{k,i}^{n+1} = a_{k,i}^n - c\Delta t D_0 a_{k,i}^n + \frac{c^2 \Delta t^2}{2} D_+ D_- a_{k,i}^n \qquad b_{k,i}^{n+1} = b_{k,i}^n + c\Delta t D_0 b_{k,i}^n + \frac{c^2 \Delta t^2}{2} D_+ D_- b_{k,i}^n \tag{75}$$

where $k = L, R$, $i = \ldots, -2, -1$ for $k = L$, and $i = 1, 2, \ldots$ for $k = R$. The normal modes are found by inserting $a_i^n = \mathcal{A}^n r^i$ and $b_i^n = \mathcal{A}^n r^i$ into (75). This leads to the characteristic equation

$$\frac{1}{2}(\nu + \nu^2) r^2 + (1 - \mathcal{A} - \nu^2) r + \frac{1}{2}(\nu^2 - \nu) = 0, \tag{76}$$

where $\nu = c\Delta t/\Delta x$ for the b characteristic component and $\nu = -c\Delta t/\Delta x$ for the a characteristic component. The assumption $c = c_L = c_R$ gives the same characteristic equation on either side of the body. There are four roots, two for the $-c$ characteristic, that we denote r_1^- and r_2^-, and two roots for the c characteristic, that we denote r_1^+ and r_2^+. It is well-known, see e.g., [6], that for the equation $u_t = c u_x$ under the CFL-condition $\lambda < 1$, the two roots of (76) satisfy

$$\begin{aligned} |r_1^+| &\leq 1 - \delta & |\mathcal{A}| &\geq 1 \\ |r_2^+| &> 1 & |\mathcal{A}| &\geq 1, \mathcal{A} \neq 1 \\ r_2^+ &= 1, & \mathcal{A} &= 1 \end{aligned} \tag{77}$$

for some $\delta > 0$ when $c > 0$, and

$$\begin{aligned} |r_1^-| &< 1 & |\mathcal{A}| &\geq 1, \mathcal{A} \neq 1 \\ r_1^- &= 1, & \mathcal{A} &= 1 \\ |r_2^-| &\geq 1 + \delta & |\mathcal{A}| &\geq 1 \end{aligned} \tag{78}$$

when $c < 0$. For the model problem (66), there are thus four roots. From (77), (78) and the condition of boundedness at infinity, it follows that the r_1^+ and r_1^- components are zero for $i < 0$ and that the r_2^+ and r_2^- components are zero for $i > 0$. Hence, the normal mode solutions to the left and to the right of the body can be written

$$\begin{bmatrix} \tilde{v} \\ \tilde{\sigma} \end{bmatrix}_{L,i} = c \begin{bmatrix} -1 \\ z \end{bmatrix} (r_2^-)^i a_{L,0} + c \begin{bmatrix} 1 \\ z \end{bmatrix} (r_2^+)^i b_{L,0} \qquad \text{for } i \leq 0 \tag{79}$$

and

$$\begin{bmatrix} \tilde{v} \\ \tilde{\sigma} \end{bmatrix}_{R,i} = c \begin{bmatrix} -1 \\ z \end{bmatrix} (r_1^-)^i a_{R,0} + c \begin{bmatrix} 1 \\ z \end{bmatrix} (r_1^+)^i b_{R,0} \qquad \text{for } i \geq 0, \tag{80}$$

respectively.

The solutions (79) and (80) inserted into the interface conditions (70), (71), (72), and (73) together with (74)

give five equations for the five unknowns $a_{R,0}, b_{R,0}, a_{L,0}, b_{L,0}$, and v_b. Fully written out these equations are

$$\left(1 + \frac{1}{r_2^-}\right) a_{L,0} - \left(1 + \frac{1}{r_2^+}\right) b_{L,0} + \frac{2}{c} v_b = 0$$
(81)

$$\left(1 + r_1^-\right) a_{R,0} - \left(1 + r_1^+\right) b_{R,0} + \frac{2}{c} v_b = 0$$
(82)

$$\left(1 + \frac{1}{r_2^-} - 2\left(\frac{\alpha}{z} + 1\right)\left(\frac{3}{2}\frac{1}{r_2^-} - \frac{1}{2}\frac{1}{(r_2^-)^2}\right)\right) a_{L,0} + \left(1 + \frac{1}{r_2^+} + 2\left(\frac{\alpha}{z} - 1\right)\left(\frac{3}{2}\frac{1}{r_2^+} - \frac{1}{2}\frac{1}{(r_2^+)^2}\right)\right) b_{L,0} - \frac{2\alpha}{z}\frac{v_b}{c} = 0$$
(83)

$$\left(1 + r_1^- + 2\left(\frac{\alpha}{z} - 1\right)\left(\frac{3}{2}r_1^- - \frac{1}{2}(r_1^-)^2\right)\right) a_{R,0} + \left(1 + r_1^+ - 2\left(\frac{\alpha}{z} + 1\right)\left(\frac{3}{2}r_1^+ - \frac{1}{2}(r_1^+)^2\right)\right) b_{R,0} + \frac{2\alpha}{z}\frac{v_b}{c} = 0$$
(84)

$$\left(\frac{\alpha}{z} + 1\right)\left(\frac{3}{2}\frac{1}{r_2^-} - \frac{1}{2}\frac{1}{(r_2^-)^2}\right) a_{L,0} + \left(1 - \frac{\alpha}{z}\right)\left(\frac{3}{2}\frac{1}{r_2^+} - \frac{1}{2}\frac{1}{(r_2^+)^2}\right) b_{L,0}$$
$$+ \left(1 - \frac{\alpha}{z}\right)\left(\frac{3}{2}r_1^- - \frac{1}{2}(r_1^-)^2\right) a_{R,0} - \left(1 + \frac{\alpha}{z}\right)\left(\frac{3}{2}r_1^+ - \frac{1}{2}(r_1^+)^2\right) b_{R,0} + \left(\frac{\mathcal{A} - 1}{\mathcal{A} + 1}\frac{2m_b}{\Delta tz} + \frac{2\alpha}{z}\right)\frac{v_b}{c} = 0$$
(85)

For the case $\alpha = z$ the system (81)-(85) becomes

$$\left(1 + \frac{1}{r_2^-}\right) a_{L,0} - \left(1 + \frac{1}{r_2^+}\right) b_{L,0} + \frac{2}{c} v_b = 0$$
(86)

$$\left(1 + r_1^-\right) a_{R,0} - \left(1 + r_1^+\right) b_{R,0} + \frac{2}{c} v_b = 0$$
(87)

$$\left(1 - \frac{5}{r_2^-} + \frac{2}{(r_2^-)^2}\right) a_{L,0} + \left(1 + \frac{1}{r_2^+}\right) b_{L,0} - \frac{2}{c} v_b = 0$$
(88)

$$\left(1 + r_1^-\right) a_{R,0} + \left(1 - 5r_1^+ + 2(r_1^+)^2\right) b_{R,0} + \frac{2}{c} v_b = 0$$
(89)

$$\left(\frac{3}{r_2^-} - \frac{1}{(r_2^-)^2}\right) a_{L,0} - \left(3r_1^+ - (r_1^+)^2\right) b_{R,0} + \left(\frac{\mathcal{A} - 1}{\mathcal{A} + 1}\frac{2m_b}{\Delta tz} + 2\right)\frac{v_b}{c} = 0$$
(90)

Theorem 3. *When $|\mathcal{A}| \geq 1$ and $\lambda < 1$, the system (86)–(90) only has the trivial solution $a_{L,0} = b_{L,0} = a_{R,0} = b_{R,0} = v_b = 0$. Hence, the numerical scheme using the interior discretizations (66), interface conditions (70)-(73), rigid body integrator (74) and projections (67)-(68) has no growing modes and is stable for $\lambda \leq 1$ and $m_b \geq 0$.*

Proof. Adding equations (86) and (88) gives

$$2\left(1 - \frac{1}{r_2^-}\right)^2 a_{L,0} = 0.$$

Because of (78),

$$\left|1 - \frac{1}{r_2^-}\right| \geq 1 - \frac{1}{|r_2^-|} \geq 1 - \frac{1}{1 + \delta} = \frac{\delta}{1 + \delta} > 0$$

and consequently, $a_{L,0} = 0$. Similarly, subtracting (87) from (89) and using (77) give $b_{R,0} = 0$. Equation (90) with $a_{L,0} = b_{R,0} = 0$ gives

$$\left(\frac{\mathcal{A} - 1}{\mathcal{A} + 1}\frac{2m_b}{\Delta tz} + 2\right)\frac{v_b}{c} = 0$$
(91)

A non-trivial solution exists if

$$\frac{\mathcal{A} - 1}{\mathcal{A} + 1}\frac{2m_b}{\Delta tz} + 2 = 0,$$

which is equivalent to $\mathcal{A} = (m_b - \Delta tz)/(m_b + \Delta tz)$. Assuming that for $\Delta t > 0$, $z > 0$, and $m_b \geq 0$, it follows that $|\mathcal{A}| < 1$, and hence that the only solution of (91) when $|\mathcal{A}| \geq 1$ is $v_b = 0$. Finally, the remaining equations

$$\left(1 + \frac{1}{r_2^+}\right) b_{L,0} = 0 \qquad \text{and} \qquad (1 + r_1^-) a_{R,0} = 0$$

have the unique solutions $b_{L,0} = a_{R,0} = 0$, because (77) and (78) exclude the possibility that $r_2^+ = -1$ or $r_1^- = -1$ when $|\mathcal{A}| \geq 1$. ☐
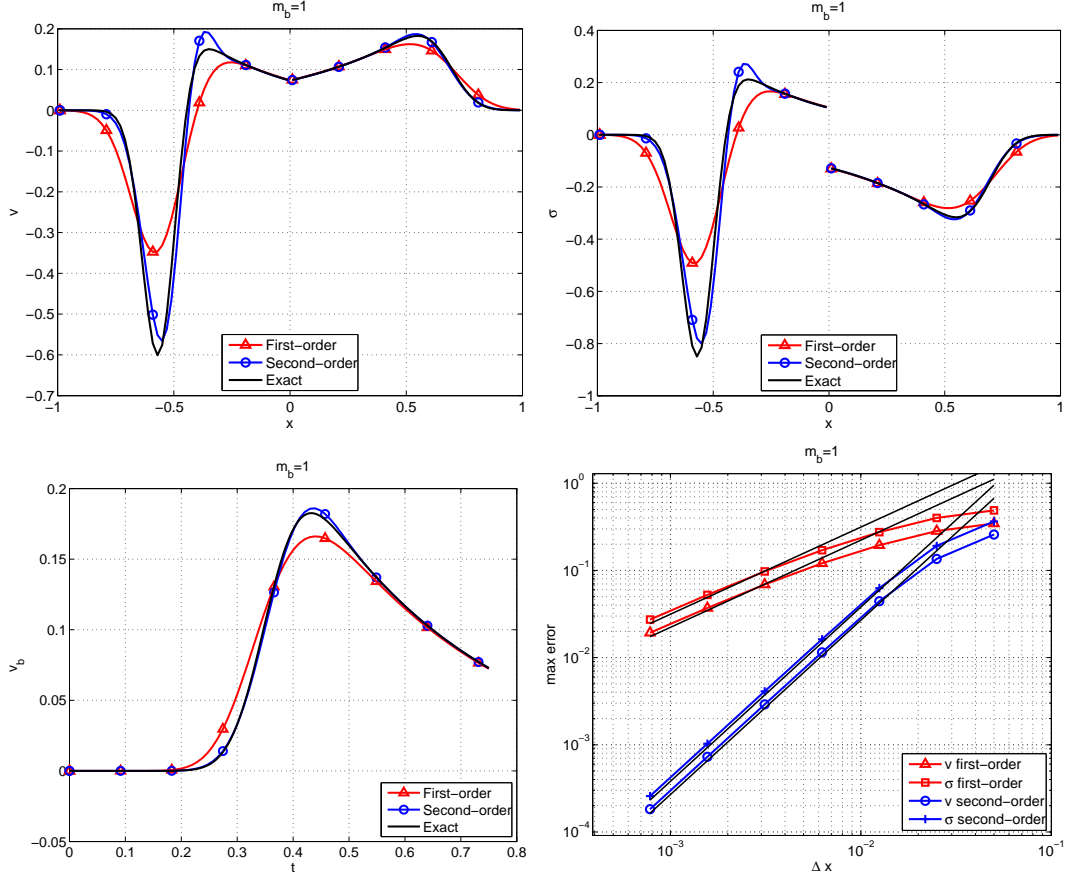
13

Figure 3: Results for the one-dimensional FSI problem with $m_b = 1$ for the first- and second-order accurate schemes. Top left: velocity at $t = 0.75$. Top-right: stress at $t = 0.75$. Bottom left: velocity of the rigid body, v_b versus time. Bottom right: convergence of the max-norms errors. The solutions are plotted in the reference domain $[-1, 0]$ for the left domain and $[0, 1]$ for the right domain with the rigid body of width $w_b = 0$ located at $x = 0$.

5. Numerical demonstration of the theory for the model problem

We now present numerical results from solving the one-dimensional FSI problem introduced in Section 3. The aim is to demonstrate the accuracy and stability of the new FSI projection algorithm For this purpose we use the exact solution derived in Appendix A. The problem consists of an initial disturbance that moves left to right and interacts with the rigid body. In the left domain the initial conditions for the velocity and stress are

$$v(x, t = 0) = \frac{c_L}{2} \exp\left(-\beta^2 (x - x_0)^2\right), \quad \sigma(x, t = 0) = -\frac{\rho_L c_L^2}{2} \exp\left(-\beta^2 (x - x_0)^2\right).$$

The rigid body is initially at rest, and the right domain has zero initial conditions. The exact solution is defined by (A.19), (A.7) and (A.10). Throughout this section we use $\rho_L = 1$, $c_L = \sqrt{2}$, $\rho_R = 1$, $c_R = \sqrt{3}$, $\beta = 10$ and $x_0 = -1/2$. Note that the initial conditions (A.17) and (A.18), and exact solutions (A.19), (A.7) and (A.10) may require differentiation with respect to space and/or time in order to be used or compared with the dependent variables of velocity and stress which we use.

5.1. Easy case: rigid body with mass one

We begin our numerical results with a case where the CFL time-step constraint in the fluids is dominant over the explicit ODE time-step constraint for the rigid body. This is the case when

$$\max(z_L, z_R) < m_b \min\left(\frac{c_L}{\Delta x_L}, \frac{c_R}{\Delta x_R}\right),$$

which implies that time steps which satisfy the usual CFL stability constraint in the fluid also satisfy the stability constraint associated with the ODE for rigid body motion. As a result, the usual coupling technique found in the

14

literature presents no problem, and we are simply setting out to demonstrate that the new projection technique does not affect the accuracy for this case.

Figure 3 shows simulation results for $m_b = 1$ when using the first-order accurate upwind scheme for the two fluid domains, the backward Euler integrator for the rigid body evolution equation, and the interface projection scheme with $\alpha = z$ as defined by Algorithm 1. In addition we show results using the second-order accurate Lax-Wendroff scheme for the fluid domains together with the trapezoidal rule for integration of the rigid body as defined by Algorithm 2 with $\alpha = z$.

For both cases $\Delta x_L = \Delta x_R = 1/50$. The exact solution and numerical approximations for v and σ are displayed as functions of the reference coordinate x at $t = 0.75$, and the velocity of the rigid body is shown as a function of time. The width of the body is taken as $w_b = 0$ (this has no influence on the results) so that the left and right reference domains meet at $x = 0$. The results from the first-order scheme show predictably smeared out solution profiles. The results from the second-order scheme are in very good agreement with the exact solution even at this coarse resolution. Figure 3 also presents results from a grid convergence study and shows the max-norm errors for this problem using the two algorithms. The predicted convergence rates are convincingly demonstrated for both velocity and stress.

Remark: For this case, one could also use the new projection scheme with a forward Euler rigid body integrator. Simulation results for this case reveal no unexpected behavior.

Remark: For this case, traditional coupling techniques without projection would not experience exponential blowup for the considered grids and time steps. Numerical results using the traditional scheme with $\alpha = 0$ for this case are nearly identical to those in Figure 3 and are therefore not shown.

5.2. Hard case: very light rigid body with mass 10^{-6}

We now move to a case where the time-step given by the usual CFL consideration is sufficiently small that the traditional algorithm with $\alpha = 0$ would experience exponential growth as discussed in analyses in Section 4. However, the time-step restriction for the new projection algorithm depends only on the time-step restrictions for each domain separately; the coupling with the rigid body imposes no new constraint on the time-step. Therefore, the time-step restriction for each fluid domain will be the standard CFL condition for that domain. The backward Euler and trapezoidal methods are both A-stable and so no additional time-step constraint is imposed by the integration of the rigid body. Consider a rigid body with mass $m_b = 10^{-6}$ and using the same grid spacings as before, $\Delta x_L = \Delta x_R = 1/50$. Figure 4 shows simulation results for this case using the two new schemes. As the figure shows, the results from the second-order scheme are predictably superior to those from the first-order scheme. The lower right graph in Figure 4 presents a convergence study. The expected rates of convergence are again convincingly demonstrated.

Remark: For this case, one could instead consider using an explicit rigid body integrator together with the projection scheme. The rigid body integration must respect the ODE time-step constraint and so subcycling can be used. It is straightforward to estimate that for $\Delta x_L = \Delta x_R = 1/50$, 14389 subcycles are required to obtain stability of a forward Euler integrator. The number of subcycles scales with the time step which decreases with increasing resolution at fixed CFL number. As a result, for $\Delta x_L = \Delta x_R = 1/1280$ (the finest resolution in the associated convergence studies), only 568 subcycles are required. Such a scheme has been implemented and the results are nearly identical to the results shown in Figure 4.

Remark: Had the traditional algorithm with $\alpha = 0$ been used, the entire solution (both fluid domains and the solid domain) would have to be integrated using a time-step which satisfies the constraint (60) or similar. For the first-order scheme with Backward Euler rigid body integrator the constraint is (60). For other fluid discretizations and/or rigid body integrators, the condition for stability can be determined in a manner similar to the methods used in Theorem 2. Such a time-step restriction can be quite severe and arises as a result of using a partitioned algorithm without projection.

5.3. Rigid body with zero mass

The new projection based FSI scheme remains well defined even when the mass of the rigid body is zero. This is apparent from the update equation for the velocity of the rigid body, equation (49) for the first-order accurate scheme or equation (74) for the second-order accurate scheme. The traditional partitioned algorithm is not well-defined for this case, since it would require division by m_b, and so is not an option. Figure 5 shows results for the first-order upwind method with backward Euler rigid body integration, and the second-order upwind method with trapezoidal rigid body integration. The exact solution is computed for $m_b = 0$ which yields essentially the same solution used for the two domain model problem in [1]. Figure 5 shows convergence results where again the predicted rates of convergence are demonstrated. No significant differences from the mass $m_b = 10^{-6}$ case in section 5.2 are observed.

Remark: For this case it is impossible to satisfy the ODE stability constraint without using an A-stable integrator and so explicit rigid body integration with subcycling is not an option. Put another way, the explicit algorithm requires an infinite number of subcycles.
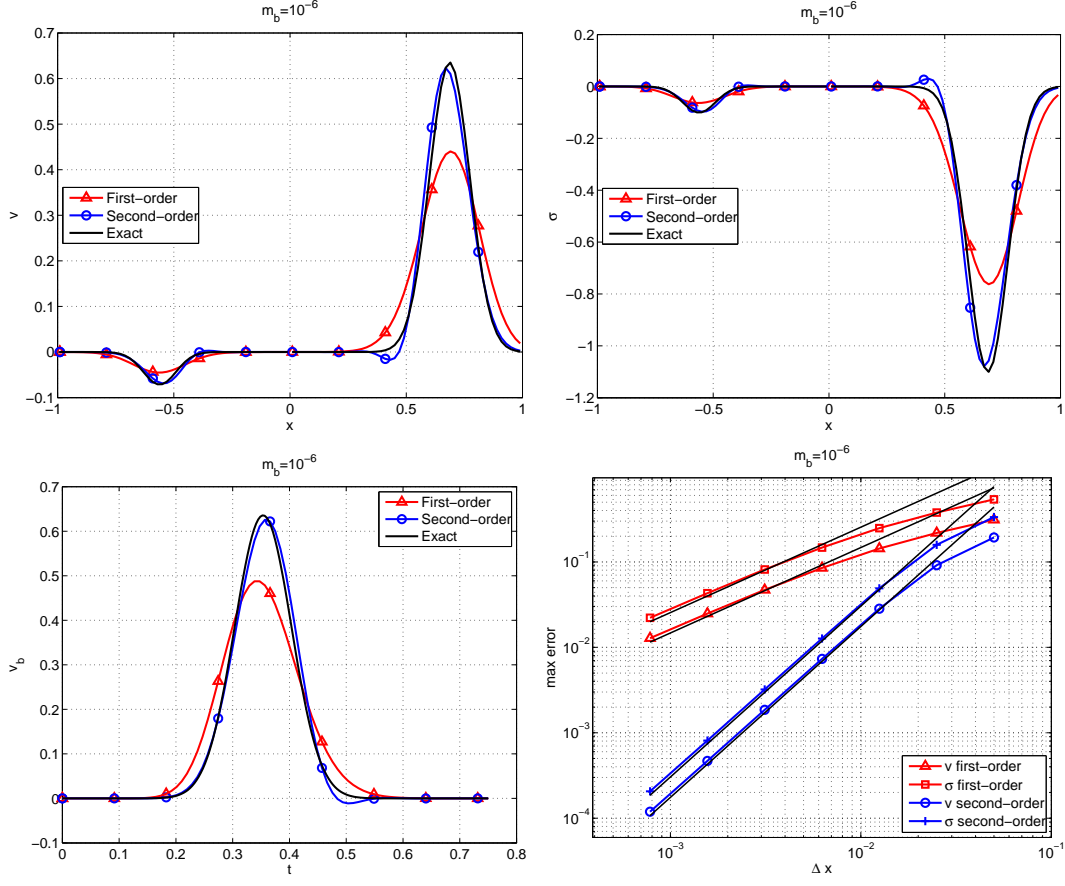
Figure 4: Results for the one-dimensional FSI problem with $m_b = 10^{-6}$ for the first- and second-order accurate schemes. Top left: velocity at $t = 0.75$. Top-right: stress at $t = 0.75$. Bottom left: velocity of the rigid body, v_b versus time. Bottom right: convergence of the max-norms errors. The solutions are plotted in the reference domain $[-1, 0]$ for the left domain and $[0, 1]$ for the right domain with the rigid body of width $w_b = 0$ located at $x = 0$.

6. The multi-dimensional interface approximation and added-mass matrices

In this section we extend the added-mass algorithm to multiple space dimensions. Formula (31) relates the pressure and velocity of a point on the body to the nearby pressure and velocity in the fluid. This relation is in a form amenable to multidimensional generalization. Let $\mathbf{r} = \mathbf{r}(t)$ denote a point on the surface of the body B, and $\mathbf{n} = \mathbf{n}(\mathbf{r}, t)$ the outward normal to the body, then in multiple space dimensions (31) becomes

$$-p(\mathbf{r}(t), t)\,\mathbf{n} = -p(\mathbf{r}+, t-)\,\mathbf{n} + z(\mathbf{r}+, t-)\left[\mathbf{n}^T\left(\mathbf{v}(\mathbf{r}+, t+) - \mathbf{v}(\mathbf{r}, t)\right)\right]\mathbf{n},$$

where $\mathbf{v}(\mathbf{r}, t) = \dot{\mathbf{r}}$ is the velocity of the point. To clarify the notation let $p_r = p(\mathbf{r}, t)$ and $\mathbf{v}_r = \mathbf{v}(\mathbf{r}, t)$ denote the pressure and velocity on the body at point $\mathbf{r} = \mathbf{r}(t)$, and $z_f = z(\mathbf{r}+, t-)$, $p_f = p(\mathbf{r}+, t-)$ and $\mathbf{v}_f = \mathbf{v}(\mathbf{r}+, t-)$ denote the impedance, pressure and velocity at the adjacent point in the fluid. This gives

$$-p_r\mathbf{n} = -p_f\mathbf{n} + z_f\left[\mathbf{n}^T\left(\mathbf{v}_f - \mathbf{v}_r\right)\right]\mathbf{n}.$$

Using equation 13 for $\mathbf{v}_r = \dot{\mathbf{r}}$ it follows that

$$-p_r\mathbf{n} = -p_f\mathbf{n} + z_f\left[\mathbf{n}^T\left(\mathbf{v}_f - \mathbf{v}_b + Y\boldsymbol{\omega}\right)\right]\mathbf{n}. \tag{92}$$

The **key point** of (92) is that is shows how the force exerted by the fluid on the body, $\mathbf{f}_s = -p_r\mathbf{n}$, depends on the velocity of the center of mass, $\mathbf{v}_b$, and the angular velocity, $\boldsymbol{\omega}$, of the body. Substituting (92) into the expressions (10)-(11) for $\boldsymbol{\mathcal{F}}$ and $\boldsymbol{\mathcal{T}}$ gives

$$\boldsymbol{\mathcal{F}} = \int_{\partial B} z_f \mathbf{n}\mathbf{n}^T(-\mathbf{v}_b + Y\boldsymbol{\omega})\,ds + \int_{\partial B} -p_f\mathbf{n} + z_f(\mathbf{n}^T\mathbf{v}_f)\mathbf{n}\,ds + \mathbf{f}_b,$$

$$\boldsymbol{\mathcal{T}} = \int_{\partial B} z_f Y \mathbf{n}\mathbf{n}^T(-\mathbf{v}_b + Y\boldsymbol{\omega})\,ds + \int_{\partial B} \mathbf{y} \times \left(-p_f\mathbf{n} + z_f(\mathbf{n}^T\mathbf{v}_f)\mathbf{n}\right)ds + \mathbf{g}_b.$$
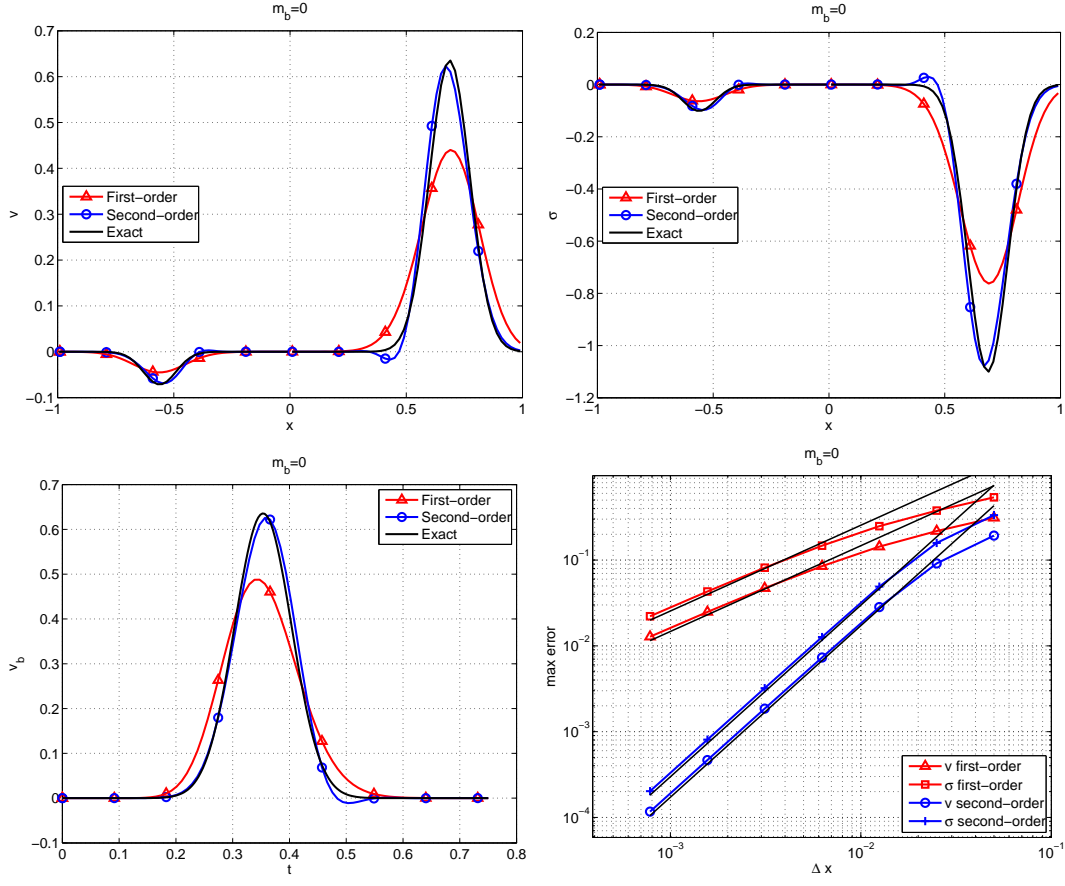
16

Figure 5: Results for the one-dimensional FSI problem with $m_b = 0$ for the first- and second-order accurate schemes. Top left: velocity at $t = 0.75$. Top-right: stress at $t = 0.75$. Bottom left: velocity of the rigid body, v_b versus time. Bottom right: convergence of the max-norms errors. The solutions are plotted in the reference domain $[-1, 0]$ for the left domain and $[0, 1]$ for the right domain with the rigid body of width $w_b = 0$ located at $x = 0$.

We write $\mathcal{F}$ and $\mathcal{T}$ in the form

$$\mathcal{F} = -A^{vv}\mathbf{v}_b - A^{v\omega}\boldsymbol{\omega} + \widetilde{\mathcal{F}},$$

$$\mathcal{T} = -A^{\omega v}\mathbf{v}_b - A^{\omega\omega}\boldsymbol{\omega} + \widetilde{\mathcal{T}}$$

where the *added-mass* matrices A^{ij} are given by (using $Y^T = -Y$, where Y is defined by (14)),

$$A^{vv} = \int_{\partial B} z_f \mathbf{n}\mathbf{n}^T \, ds, \qquad A^{v\omega} = \int_{\partial B} z_f \mathbf{n}(Y\mathbf{n})^T \, ds, \tag{93}$$

$$A^{\omega v} = \int_{\partial B} z_f (Y\mathbf{n})\mathbf{n}^T \, ds \qquad A^{\omega\omega} = \int_{\partial B} z_f Y\mathbf{n}(Y\mathbf{n})^T \, ds, \tag{94}$$

and $\widetilde{\mathcal{F}}$ and $\widetilde{\mathcal{T}}$ are given by

$$\widetilde{\mathcal{F}} = \int_{\partial B} -p_f \mathbf{n} + z_f(\mathbf{n}^T\mathbf{v}_f)\mathbf{n} \, ds + \mathbf{f}_b, \tag{95}$$

$$\widetilde{\mathcal{T}} = \int_{\partial B} \mathbf{y} \times \big(-p_f \mathbf{n} + z_f(\mathbf{n}^T\mathbf{v}_f)\mathbf{n} \big) \, ds + \mathbf{g}_b. \tag{96}$$

Note that A^{vv} and $A^{\omega\omega}$ are symmetric and positive semi-definite while $(A^{v\omega})^T = A^{\omega v}$. Let $A_m \in \mathbb{R}^{6\times6}$ denote the composite added mass matrix (tensor),

$$A_m = \begin{bmatrix} A^{vv} & A^{v\omega} \\ A^{\omega v} & A^{\omega\omega} \end{bmatrix}.$$

17

This matrix is symmetric and positive semi-definite since for any vector $\mathbf{w} = [\mathbf{a} \ \mathbf{b}]^T \in \mathbb{R}^6$, $\mathbf{a} \in \mathbb{R}^3$, $\mathbf{b} \in \mathbb{R}^3$

$$\mathbf{w}^T A_m \mathbf{w} = [\mathbf{a} \ \mathbf{b}] \begin{bmatrix} A^{vv} & A^{v\omega} \\ A^{\omega v} & A^{\omega\omega} \end{bmatrix} \begin{bmatrix} \mathbf{a} \\ \mathbf{b} \end{bmatrix} = \int z_f \Big(\|\mathbf{n}^T \mathbf{a}\|^2 + 2(\mathbf{n}^T \mathbf{a})(Y\mathbf{n})^T \mathbf{b} + \|(Y\mathbf{n})^T \mathbf{b}\|^2 \Big) ds,$$

$$= \int z_f \Big((\mathbf{n}^T \mathbf{a}) + (Y\mathbf{n})^T \mathbf{b} \Big)^2 ds.$$

The rigid body equations of motion (5)-(8) can now be written in the form

$$\begin{bmatrix} I & 0 & 0 & 0 \\ 0 & m_b I & 0 & 0 \\ 0 & 0 & A & 0 \\ 0 & 0 & 0 & I \end{bmatrix} \begin{bmatrix} \dot{\mathbf{x}}_b \\ \dot{\mathbf{v}}_b \\ \dot{\boldsymbol{\omega}} \\ \dot{E} \end{bmatrix} + \begin{bmatrix} 0 & -I & 0 & 0 \\ 0 & A^{vv} & A^{v\omega} & 0 \\ 0 & A^{\omega v} & A^{\omega\omega} - WA & 0 \\ 0 & 0 & 0 & -W \end{bmatrix} \begin{bmatrix} \mathbf{x}_b \\ \mathbf{v}_b \\ \boldsymbol{\omega} \\ E \end{bmatrix} = \begin{bmatrix} 0 \\ \widetilde{\boldsymbol{\mathcal{F}}} \\ \widetilde{\boldsymbol{\mathcal{T}}} \\ 0 \end{bmatrix}. \tag{97}$$

We will refer to equations (97) as the *added-mass* Newton-Euler equations.

Remark: By solving equations (97) with an implicit time-stepping scheme that treats the added-mass terms implicitly, the rigid body equations can be advanced with a *large* time step even as m_b and A approach zero, *provided* A_m is nonsingular. This is described in more detail in Section 7.

Remark: In Appendix B we present the form of the added-mass matrices for some common body shapes.

7. The multi-dimensional time-stepping algorithm

We make use of overlapping grids to treat multi-dimensional problems with moving rigid bodies. Narrow boundary fitted grids lie next to the bodies and these move with the bodies (see the examples in Section 8). One or more stationary background grids generally cover most of the domain. This approach results in high-quality grids even as bodies undergo large motions. The time-stepping algorithm we use for FSI problems with rigid bodies is described in detail in [7], while that for FSI problems with deforming solids is described in [2]. In [7] the Newton-Euler equations for the rigid bodies are solved using a Leap-frog predictor step followed by a trapezoidal rule corrector step.

The FSI time stepping algorithm			
Stage	Condition	Type	Assigns
Predict(a)	Predict body motion, moving grid	extrapolation	$\mathbf{x}_b^p, \mathbf{v}_b^p, \boldsymbol{\omega}^p, \mathbf{E}^p, \mathbf{G}_{\mathbf{i}}^p$
Predict(b)	Advance fluid $\mathbf{w}_{\mathbf{i}}^n, \mathbf{w}_{\mathbf{i}}^p$,	PDE	$\mathbf{w}_{\mathbf{i}}^n, \mathbf{i} \in \mathcal{I}_I, \quad \mathbf{w}_{\mathbf{i}}^p, \mathbf{i} \in \mathcal{I}_B$
Body(a)	Compute added mass terms (93)-(96)		$A_{11}^p, A_{12}^p, A_{21}^p, A_{22}^p, \widetilde{\boldsymbol{\mathcal{F}}}^p, \widetilde{\boldsymbol{\mathcal{T}}}^p$
Body(b)	Advance rigid body (97)	ODEs	$\mathbf{x}_b^n, \mathbf{v}_b^n, \boldsymbol{\omega}^n, \mathbf{E}^n$
Correct(a)	Project fluid on body (98)-(100)	projection	$\mathbf{v}_{\mathbf{i}}^n, p_{\mathbf{i}}^n, \rho_{\mathbf{i}}^n, \quad \mathbf{i} \in \mathcal{I}_B$
Correct(b)	Correct moving grid	projection	$\mathbf{G}_{\mathbf{i}}^n$
Ghost	Assign fluid ghost values	PDE, extrapolation	$\mathbf{w}_{\mathbf{i}}^n, \quad \mathbf{i} \in \mathcal{I}_G$

Figure 6: The FSI time stepping algorithm for advancing the states of the fluid and rigid body.

For the new interface algorithm developed here, we require an implicit time-stepping scheme to solve the Newton-Euler equations with added mass terms (97) and we have chosen to use diagonally implicit Runge-Kutta (DIRK) schemes for this purpose [20]. DIRK schemes have very nice stability and accuracy properties. The one-stage, first-order accurate DIRK scheme, which we denote by DIRK1, is just the backward-Euler scheme. For the numerical results in section 8 we will use a two-stage third-order accurate (A-stable) scheme, denoted by DIRK3, due to Crouzeiux (see [20] (2.2)). In each stage of the DIRK scheme we solve an implicit approximation to (97) by Newton's method.
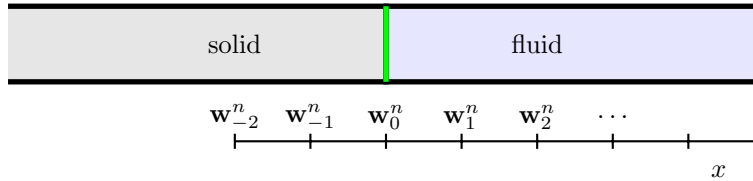

Figure 7: The fluid grids for two-dimensional problems have a grid point aligned with the boundary of the rigid body. The solution on the boundary is $\mathbf{w}_0^n$, while $\mathbf{w}_{-2}^n$ and $\mathbf{w}_{-1}^n$ denote the values on the ghost points. For clarity, only one grid line is shown in the direction normal to the boundary.

The FSI time stepping algorithm for advancing the fluid and rigid body is outlined in Figure 6. In a slight difference from the grid arrangement used for the analysis in one-dimension as illustrated in Fig.2, the two-dimensional grids

have a grid point aligned with the boundary of the body as shown in Fig.7. Let $\mathbf{w_i}^n = (\rho_\mathbf{i}^n, \mathbf{v_i}^n, p_\mathbf{i}^n)$ denote the discrete solution in space and time for the state of the fluid at time t^n, where $\mathbf{i}$ is a multi-index. Let $(\mathbf{x}_b^n, \mathbf{v}_b^n, \boldsymbol{\omega}^n, \mathbf{E}^n)$ denote the discrete approximation in time to the state of the rigid body. Let $\mathbf{x_i}^n = \mathbf{G_i}^n$ denote the (moving) grid points on the fluid grid that lies next to the body and $\dot{\mathbf{G}}_\mathbf{i}^n$ the grid velocity (the fluid domain will actually be discretized with multiple overlapping grids but for clarity we ignore these other grids in the current discussion).

Suppose that we are given the full state of the discrete solution at time t^{n-1} and wish to determine the state at the next time step t^n. In the first stage of the time stepping algorithm, predicted values are obtained for the state of the solid body at the new time, $(\mathbf{x}_b^p, \mathbf{v}_b^p, \boldsymbol{\omega}^p, \mathbf{E}^p)$. These values can be obtained either from the Newton-Euler equations of motion or using extrapolation in time (for a second order accurate scheme we extrapolate using the current level and two previous time levels). From the predicted state of the body we can obtain predicted values for the grid location, $\mathbf{G}_\mathbf{i}^p$, and grid velocity, $\dot{\mathbf{G}}_\mathbf{i}^p$; these values are needed to advance the fluid state. Note that the grids move as a rigid body and do not deform. In the second stage of the time stepping algorithm we obtain the new values of the fluid state $\mathbf{w_i}^n = (\rho_\mathbf{i}^n, \mathbf{v_i}^n, p_\mathbf{i}^n)$ at interior grid points, $\mathbf{i} \in \mathcal{I}_I$, and predicted values, $\mathbf{w_i}^p = (\rho_\mathbf{i}^p, \mathbf{v_i}^p, p_\mathbf{i}^p)$, at points on the body surface, $\mathbf{i} \in \mathcal{I}_B$. These values are obtained from our high-order Godunov-based upwind scheme [7]. Note that at this stage we do not impose any boundary conditions on the fluid at the body surface. Predicted values of the fluid on the body, $\mathbf{i} \in \mathcal{I}_B$, can be obtained, however, since the fluid state contains ghost points, $\mathbf{i} \in \mathcal{I}_G$ (two lines of ghost points being used for our second-order Godunov scheme). Given the predicted fluid states $\mathbf{w_i}^p$ we can compute the partial body forces (95)-(96) and the added mass matrices (93)-(93) using numerical integration over the surface of the body. We then solve the added-mass Newton-Euler equations (97) (e.g. with a DIRK scheme) to determine the corrected state of the rigid-body at the new time, $(\mathbf{x}_b^n, \mathbf{v}_b^n, \boldsymbol{\omega}^n, \mathbf{E}^n)$. The predicted state of the fluid on the solid body is then corrected by setting the fluid velocity equal to the (local) body velocity and the fluid pressure to equal its projected value,

$$\mathbf{v_i}^n = \mathbf{v}_{b,\mathbf{i}}^n, \qquad\qquad \mathbf{i} \in \mathcal{I}_B, \tag{98}$$

$$-p_\mathbf{i}^n = -p_\mathbf{i}^p + z^p \mathbf{n}^T (\mathbf{v_i}^p - \mathbf{v}_{b,\mathbf{i}}^n), \quad \mathbf{i} \in \mathcal{I}_B. \tag{99}$$

Here the local body velocity is $\mathbf{v}_{b,\mathbf{i}} = \mathbf{v}_b^n + W^n(\mathbf{r_i}^n - \mathbf{x}_b^n)$, where $\mathbf{r_i}^n$ denotes the location of a point on the body surface, and where W^n is defined from $\boldsymbol{\omega}^n$ using (9). After projecting the pressure, the density is corrected using

$$\rho_\mathbf{i}^n = \rho_\mathbf{i}^p \left(p_\mathbf{i}^n / p_\mathbf{i}^p \right)^{1/\gamma}, \qquad \mathbf{i} \in \mathcal{I}_B, \tag{100}$$

which ensures that the entropy of the predicted state equals that of the corrected state. The fluid grid, $\mathbf{G}_\mathbf{i}^n$, and grid velocity, $\dot{\mathbf{G}}_\mathbf{i}^n$, at the new time are corrected from the predicted values to match the new state of the rigid body. In the final stage of the time stepping algorithm, the ghost values of fluid state that lie adjacent to the body surface are updated using the appropriate boundary conditions and compatibility conditions, see [7, 2] for more details.

8. Numerical results in two space dimensions

In this section we present numerical results in two-dimensions that demonstrate the accuracy and stability of the added-mass interface algorithm when applied to light rigid bodies. A pressure driven light piston problem is used to examine the accuracy of the two-dimensional added-mass algorithm for an FSI problem with an analytic solution. A smoothly accelerated light rigid body in the shape of an ellipse is used to evaluate the scheme for a two-dimensional problem that includes the rotational added-mass terms. Solutions using the new added-mass algorithm are compared to the old algorithm, which is necessarily run at a small CFL number to avoid exponential blowup. Although the exact solution to this problem is not known, a posteriori estimates of the errors are determined from solutions on a sequence of grids of increasing resolution. As a final example we simulate a Mach 2 shock impacting an ellipse of zero mass and zero moment of inertia. This case demonstrates the robustness of the added-mass algorithm for a very difficult situation. Solutions to this shock driven ellipse problem are computed at varying grid resolutions and compared. These results include computations that use dynamic adaptive mesh refinement (AMR).

8.1. Pressure driven light piston

The geometry of the one-dimensional pressure driven piston problem is shown in Fig. 8 A compressible fluid occupying the region $x > G(t)$ lies adjacent to a piston of mass m_b and cross-sectional area $\mathcal{A}_b$. The face of the piston that lies next to the fluid follows the curve $x = G(t)$ as time evolves. A body force $f_b(t)$ also acts on the piston. The exact solution to this problem can be determined for a fluid that is initially at rest and the form of this solution is given in [7]. When $f_b(t) = 0$, the exact solution can be determined explicitly. For general $f_b(t)$, the case considered here, the exact solution can be accurately approximated by numerical integration of the appropriate ordinary differential equations.

We solve the pressure driven piston problem on a two-dimensional overlapping grid denoted by $\mathcal{G}_p^{(j)}$, where j denotes the grid resolution (see Figure 8). The grid spacing in the x-direction is chosen to be $\Delta x^{(j)} = 1/(10j)$. The spacing in the y-direction is held fixed at $\Delta y = 2/10$. A background Cartesian grid covers the domain $[-0.5, 1.5] \times [0, 1]$
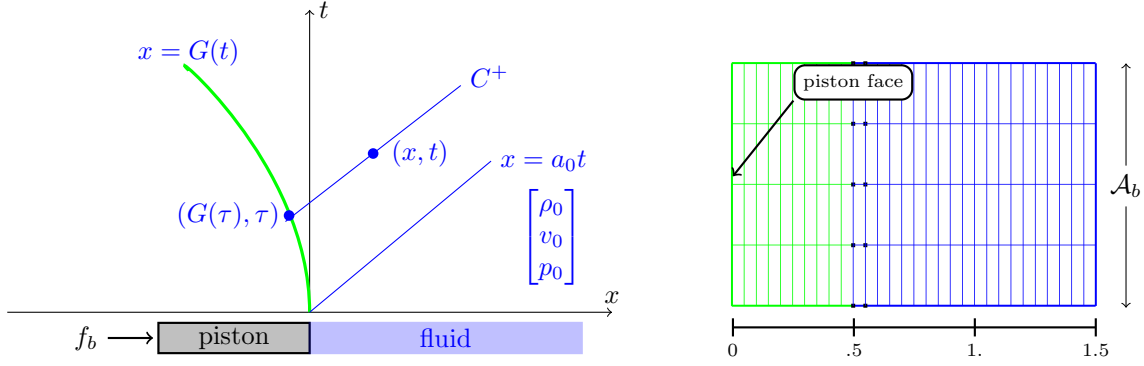
Figure 8: Left: the x-t diagram for the pressure driven piston problem with a receding piston. Right: overlapping grid $\mathcal{G}_p^{(2)}$ for the fluid region at $t = 0.0$. The green grid moves with the piston. The blue background grid does not move. The interpolation points are marked as black dots.

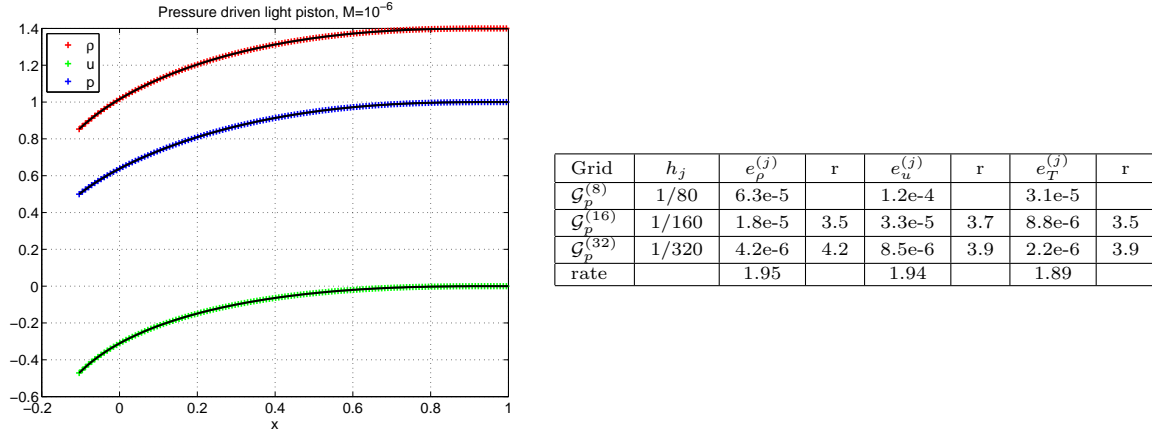| Grid	h_j	$e_\rho^{(j)}$	r	$e_u^{(j)}$	r	$e_T^{(j)}$	r
$\mathcal{G}_p^{(8)}$	1/80	6.3e-5		1.2e-4		3.1e-5	
$\mathcal{G}_p^{(16)}$	1/160	1.8e-5	3.5	3.3e-5	3.7	8.8e-6	3.5
$\mathcal{G}_p^{(32)}$	1/320	4.2e-6	4.2	8.5e-6	3.9	2.2e-6	3.9
rate		1.95		1.94		1.89	

Figure 9: Results for a pressure driven light piston of mass $m_b = 10^{-6}$. Left: computed and exact solution at $t = 1$. using $\mathcal{G}_p^{(8)}$. Right: maximum errors and estimated convergence rates at time $t = 1$.

and remains stationary. A second Cartesian grid initially covers the domain $[0, 0.5] \times [0, 1]$ and moves over time according the piston motion.

The pressure driven piston problem is solved for a piston of mass $m_b = 10^{-6}$. The initial conditions for the fluid are $(\rho_0, v_0, p_0) = (1.4, 0., 1)$ with $\gamma = 1.4$. The body force is chosen to be $f_b(t) = p_0 \mathcal{A}_b (1 - \frac{1}{2}t^3)$ which results in a piston that smoothly recedes to the left and for which we expect the numerical solution to be second-order accurate in the max-norm. The computed and exact solutions are shown in Fig.9 for results using grid $\mathcal{G}_p^{(8)}$ and these are in excellent agreement. Figure 9 also gives the max-norm errors for solutions computed on a sequence of grids of increasing resolution. The values in the columns labelled "r" give the ratio of the error on the current grid to that on previous coarser grid, a ratio of 4 being expected for a second-order accurate method. The convergence rate, β, is estimated from a least-squares fit to the log of the error equation $e(h) = Ch^\beta$. The results show that the solution is converging at close to second-order.

8.2. Smoothly accelerated ellipse

In this example we consider a light rigid body in the shape of an ellipse that is accelerated by a smoothly varying body force. We compare the solution from the new added-mass algorithm to that from the old algorithm, the latter requiring a very small time step to avoid exponential blowup when the mass of the body is small.

The overlapping grid for this *rotated-ellipse* problem is denoted by $\mathcal{G}_{re}^{(j)}$ where j denotes the grid resolution (grid $\mathcal{G}_{re}^{(1)}$ is shown in Figure 10). The grid consists on a stationary background Cartesian grid for the region $[-2, 2] \times [-2, 2]$, with grid spacing $\Delta s^{(j)} = 1/(10j)$. A narrow boundary fitted grid is located next to the surface of the elliptical body, and this grid will move to follow the motion of the body. The surface of the body is defined by an ellipse, which has major and minor axes of lengths 1.4 and 0.7, respectively, and which is rotated by $\pi/4$ in the counterclockwise direction. The boundary fitted grid extends 8 grid lines in the normal direction (the grid in Figure 10 shows an additional ghost line), and the grid spacing in the normal direction is slightly clustered near the ellipse surface. The number of points in the tangential direction is chosen so the grid spacing is approximately $\Delta s^{(j)}$.

The ellipse is accelerated using a body force that smoothly ramps from zero to one on the time interval $[0, \frac{1}{2}]$ and then smoothly ramps back to zero over the interval $[\frac{1}{2}, 1]$. In particular, the body force is in the x-direction and is
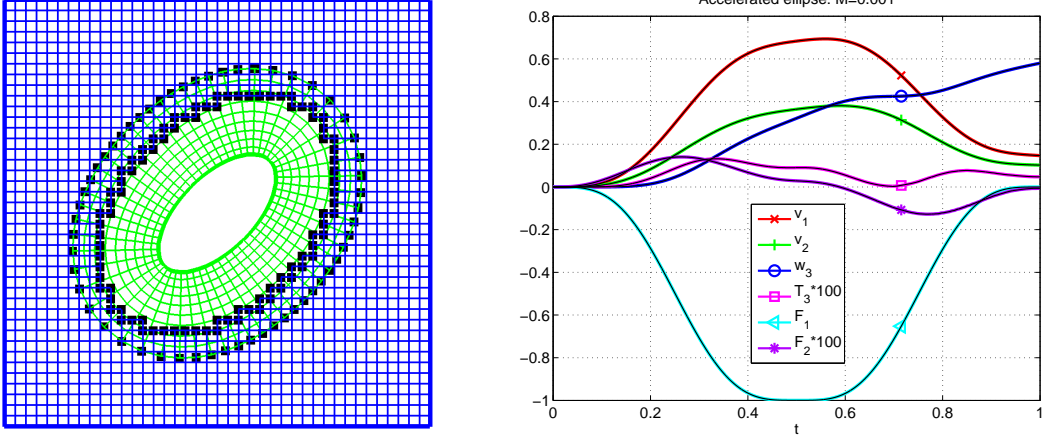
Figure 10: Accelerated ellipse. Left: overlapping grid $\mathcal{G}_{\mathrm{re}}^{(1)}$ at time $t = 0$. Right: time histories of the rigid body velocity (v_1, v_2), angular momentum w_3, torque T_3 and forces (F_1, F_2) for an ellipse of mass $m_b = 10^{-3}$ and moment of inertial $I_3 = 10^{-3}$ using the old algorithm (black lines) and new algorithm (using grid $\mathcal{G}_{\mathrm{re}}^{(2)}$). ($T_3$ and F_2 are scaled by a factor of 100 for graphical purposes) . The force shown on the body does not include the contribution from the external body force.

given by

$$f_x(t) = R(2t) - R(2t - 1), \quad \text{where,} \quad R(t) = \begin{cases} 0 & \text{if } t \leq 0 \\ 35t^4 - 84t^5 + 70t^6 - 20t^7 & \text{if } 0 < t < 1 \\ 1 & \text{if } t \geq 0 \end{cases} . \tag{101}$$

Note that the ramp function R has three continuous derivatives since the first three derivatives of $R(t)$ are zero at $t = 0$ and $t = 1$.

We consider an an ellipse of mass $m_b = 10^{-3}$ and moment of inertia $I_3 = 10^{-3}$. The fluid is taken as an ideal gas with $\gamma = 1.4$. The ellipse and fluid are initially at rest with the initial fluid state given by $(\rho, v_1, v_2, p) = (1/\gamma, 0, 0, 1)$. The smooth body force is given by (101). The boundary conditions on the Cartesian grid, which have little influence for this problem, are inflow on the left with all variables given, outflow on the right side (all variables extrapolated) and slip walls on the top and bottom. For comparison, we solve this problem using both the old FSI algorithm and the new *added-mass* FSI algorithm. The new algorithm is run at a CFL number of 0.9. The old algorithm experiences exponential blowup at this CFL number and is instead run at a CFL number of 1/100.

In the right-hand side of Figure 10 we show the state of the rigid body over time for the old and new algorithms. The body initially accelerates upward and to the right as indicated by the components of the body velocity and rotates in a counter-clockwise direction as indicated by the angular velocity. The forces on the body shown in Figure 10 do not include the contributions from the external body force and thus represent the force exerted by the fluid on the body. The force f_1 indicates that the fluid pushes back on the body to nearly balance the external force. The results from the old and new algorithm are nearly indistinguishable in this plot indicating that the new algorithm provides an accurate approximation even with a time step that is nearly 100 times larger than the old algorithm.

Figure 11 shows contours of the pressure field at times $t = 0.5$ and $t = 1.0$ for both the old and new algorithms. The accelerating body generates a forward moving wave that steepens over time and which has formed a shock by $t = 1.0$. The solutions from the old and new algorithm are in excellent agreement with almost no detectable differences. For a more quantitative evaluation of the accuracy we determine a a-posteriori error estimates by solving the problem on a sequence of grids of increasing resolution and using the error estimation approach described in [21, 22]. Figure 12 shows the estimated max-norm errors and convergence rates at time $t = 0.4$ when the solution is still smooth. These results show that the solution is converging at close to second-order accuracy. We note that for these results the slope-limiter was turned off in the Godunov method since this slope limiter can reduce the order of accuracy. Figure 13 shows the estimated L_1-norm errors and convergence rates at time $t = 1.0$ when the solution is no longer smooth. In this case the results show that the solution is converging at rates close to 1, which are the expected rates for problems with shocks. We note that the discrete L_1-norm of a grid function is computed in the usual way by summing the absolute values of the values at each grid point and dividing by the total number of grid points [21].

8.3. Shock driven zero mass ellipse

The shock driven ellipse problem consists of a Mach 2 shock that impacts an ellipse of zero mass and zero moment of inertia. This example demonstrates the robustness of the new added-mass algorithm on a difficult problem for which the old rigid-body FSI algorithm would fail for any time-step, no matter how small. We note that since
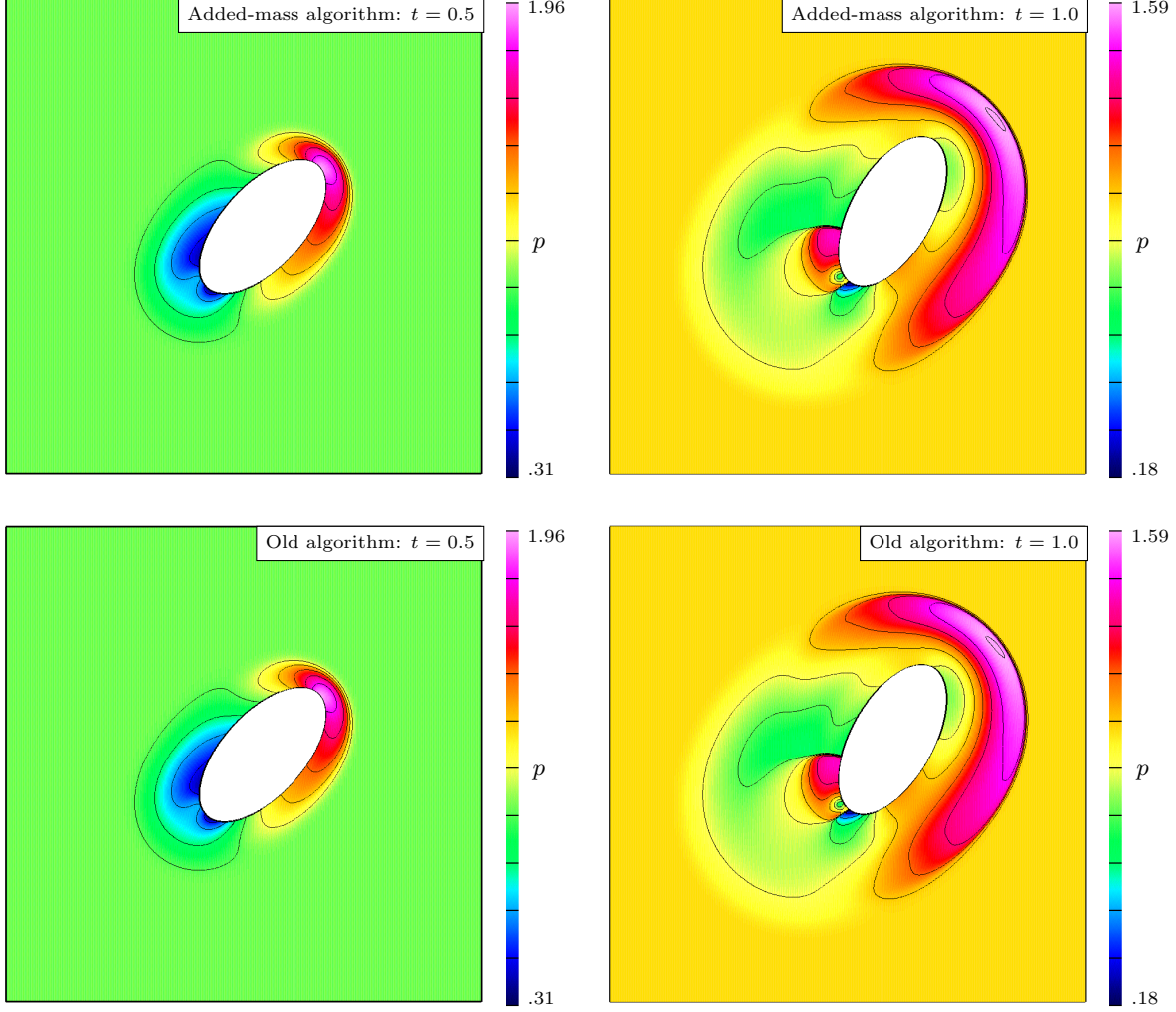
Figure 11: Accelerated ellipse: pressure at $t = 0.5$ and $t = 1.0$ for the old algorithm running at CFL number 10^{-2} (bottom) and new *added-mass* algorithm running at CFL number 0.9 (top) for grid $\mathcal{G}_{\text{re}}^{(16)}$.

Grid $\mathcal{G}^{(j)}$	h_j	$e_\rho^{(j)}$	r	$e_u^{(j)}$	r	$e_v^{(j)}$	r	$e_p^{(j)}$	r
$\mathcal{G}_{\text{re}}^{(8)}$	1/40	8.0e-3		5.3e-3		3.4e-3		8.3e-3	
$\mathcal{G}_{\text{re}}^{(16)}$	1/80	2.2e-3	3.7	1.4e-3	3.8	9.7e-4	3.5	2.3e-3	3.7
$\mathcal{G}_{\text{re}}^{(32)}$	1/160	5.9e-4	3.7	3.7e-4	3.8	2.8e-4	3.5	6.2e-4	3.7
rate		1.88		1.93		1.80		1.87	

Figure 12: A posteriori estimated errors (max-norm) and convergence rates for the accelerated ellipse at $t = 0.4$ (no slope limiter). The scheme converges at close to second-order accuracy in the max-norm when the solution is smooth.

the mass and moments of inertial of the body are zero in the Newton-Euler equations (97), the linear and angular velocities of the body respond immediately to ensure the net force on the body is zero; there is no damping in the response from the body's inertia.

The overlapping grid for this problem, $\mathcal{G}_{\text{re}}^j$ is the same as that used in Section 8.2. We use adaptive mesh refinement in some of the computations of this section. Let $\mathcal{G}_{\text{re}}^{j \times 4}$ denote the AMR grid that has a base grid $\mathcal{G}_{\text{re}}^j$ with grid spacing $\Delta s^{(j)} \approx 1/(10j)$ together with one level of refinement grids of refinement factor 4. The effective resolution of the AMR grid $\mathcal{G}_{\text{re}}^{j \times 4}$ is thus $\Delta s^{(j \times 4)} \approx 1/(40j)$. We note that the AMR grids are added to both the background grid and to the component grid around the ellipse, refer to [7] for further details of the moving-grid AMR approach.

The initial conditions in the fluid consist of a shock located at $x = -1$ with initial state $(\rho, u, v, p) = (2.6667, 1.25, 0, 3.214256)$ ahead of the shock and $(\rho, u, v, p) = (1, 0, 0, 1.4)$ behind the shock. The boundary conditions are supersonic inflow (all variables specified) on the left face of the background grid and supersonic outflow

Grid $\mathcal{G}^{(j)}$	h_j	$e_\rho^{(j)}$	r	$e_u^{(j)}$	r	$e_v^{(j)}$	r	$e_p^{(j)}$	r
$\mathcal{G}_{\mathrm{re}}^{(8)}$	1/40	2.1e-3		9.3e-4		9.6e-4		2.1e-3	
$\mathcal{G}_{\mathrm{re}}^{(16)}$	1/80	9.9e-4	2.1	4.3e-4	2.1	4.6e-4	2.1	9.6e-4	2.2
$\mathcal{G}_{\mathrm{re}}^{(32)}$	1/160	4.7e-4	2.1	2.0e-4	2.1	2.2e-4	2.1	4.5e-4	2.2
rate		1.08		1.09		1.07		1.11	

Figure 13: A posteriori estimated errors (L_1-norm) and convergence rates for the accelerated ellipse at $t = 1.0$. The scheme converges at close to first-order accuracy in the L_1-norm when the solution is not smooth.

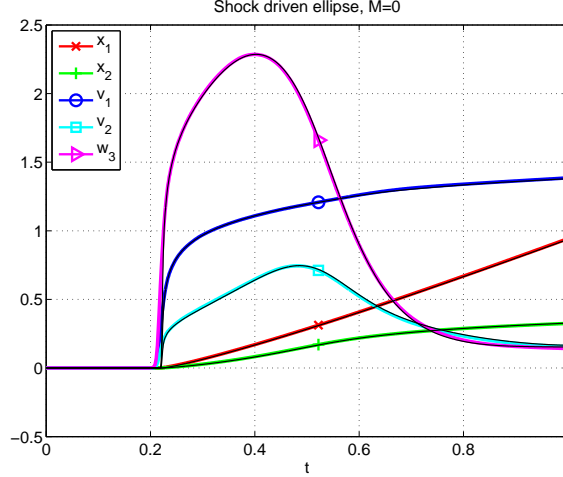(all variables extrapolated) on the other faces of the background grid.

Figure 14: Shock-drive ellipse: time histories of the center of mass, (x_1, x_2), the velocity of the center of mass, (v_1, v_2) and the angular velocity w_3. The colored lines are results from the coarse grid $\mathcal{G}_{\mathrm{re}}^{(8)}$ while the black lines are results using the finer grid $\mathcal{G}_{\mathrm{re}}^{(32)}$.

Figure 14 compares the time history of the rigid body dynamics from a coarse grid, $\mathcal{G}_{\mathrm{re}}^{(8)}$, and finer grid, $\mathcal{G}_{\mathrm{re}}^{(8)}$, computation. The velocity and angular velocity are seen to rapidly increase when the shock first hits the ellipse just after $t = 0.2$. The ellipse is initially accelerated up and to the right and experiences a rapid counter-clockwise rotation. After an initial rise, the angular velocity decreases and approximately levels off at some positive value[3]. The results from the two computations are in excellent agreement.

Numerical schlieren and contours of the pressure field at different times are shown in Figure 15 (see [7] for a definition of the numerical schlieren function). The computations were performed with AMR using the grid $\mathcal{G}_{\mathrm{re}}^{(16 \times 4)}$ (base grid $\mathcal{G}_{\mathrm{re}}^{(16)}$ plus one refinement level of refinement ratio 4). The solution at $t = 0.4$ shows the ellipse has undergone a rapid acceleration upward and to the right combined with a rapid counter clockwise rotation. The impact of the incident shock on the ellipse causes a shock to form in the region ahead of the body. By $t = 1.0$, a complex pattern of interacting shocks has formed in the regions above and below the ellipse. In Figure 16 we compare the schlieren images of the solution at $t = 1.0$ from grids of different resolutions. These result show good agreement in the basic structure of the solution, with additional fine scale features appearing as the grid is refined. This is the expected behavior for inviscid computations.

---

[3]We note that the long time behavior of the ellipse is of interest but we do not pursue that line of investigation here.
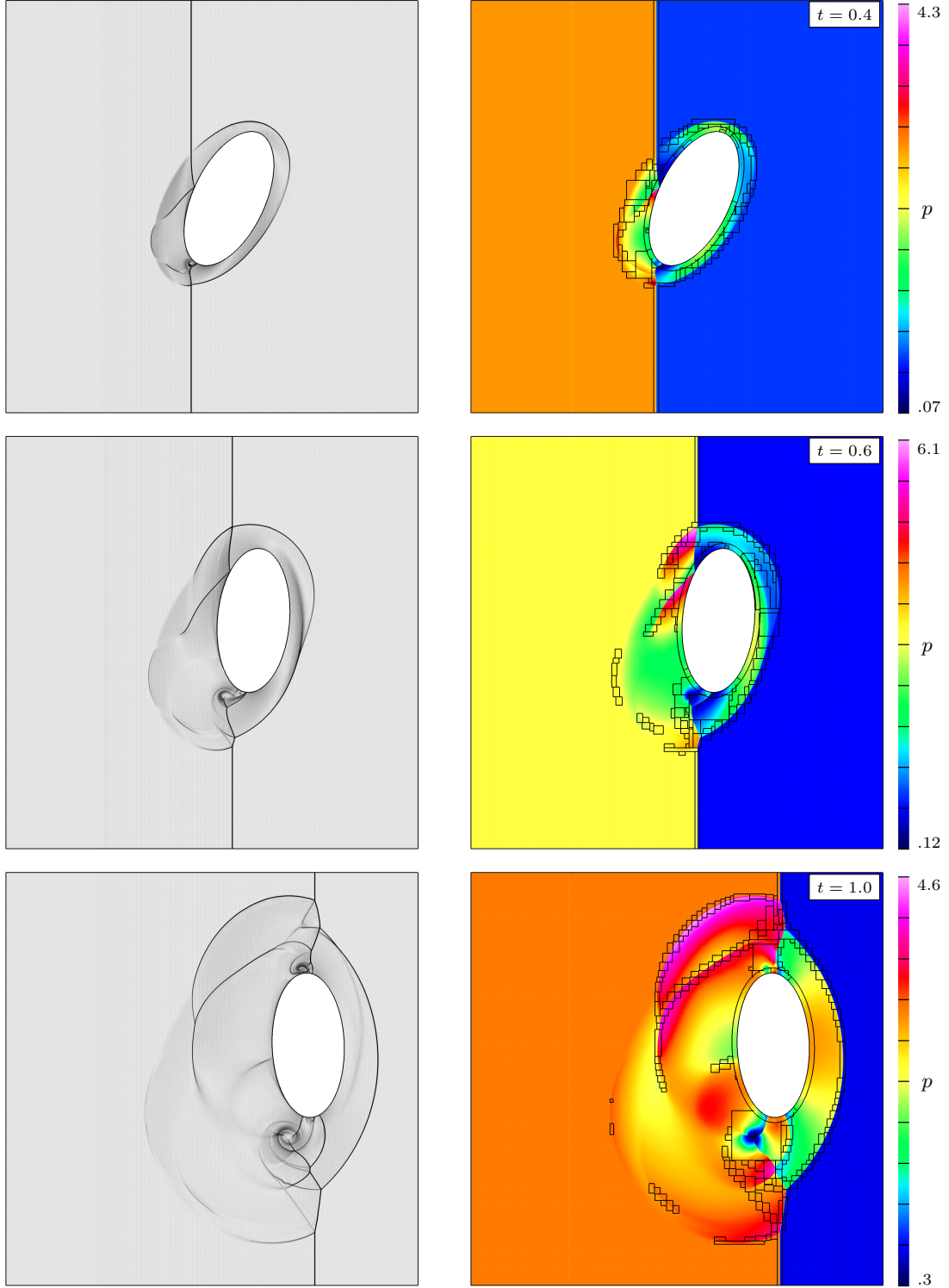
Figure 15: Shock driven zero mass ellipse. Schlieren images (left column) and pressure contours (right column) at times $t = 0.4$, $t = 0.6$ and $= 1.0$ using grid $\mathcal{G}_{\mathrm{re}}^{(16 \times 4)}$. The block boundaries of the refinement grids are shown superimposed on the pressure contours.
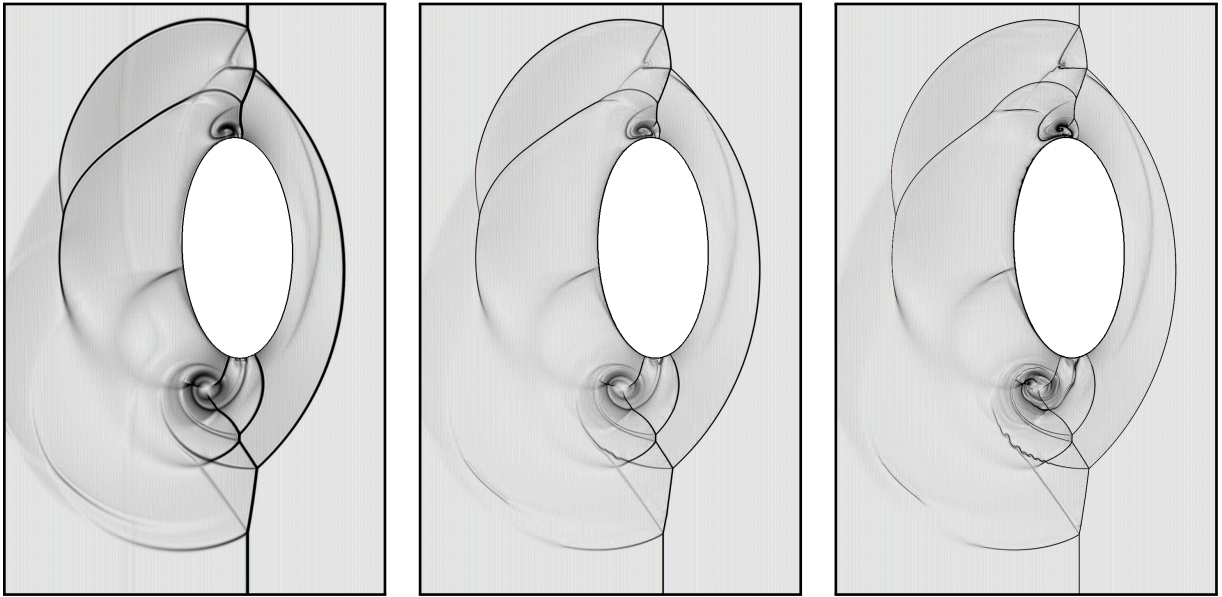
Figure 16: Shock driven zero mass ellipse. A comparison of schlieren images of the solution at $t = 1.0$ computed on the coarse grid $\mathcal{G}_{\text{re}}^{(32)}$ (left), medium grid $\mathcal{G}_{\text{re}}^{(16 \times 4)}$ (middle) and fine (AMR) grid $\mathcal{G}_{\text{re}}^{(8 \times 4 \times 4)}$ (right).

9. Conclusions

We have presented a stable partitioned scheme for the coupling of light rigid bodies with inviscid compressible fluids. This new *added-mass* scheme, derived from an analysis of a fluid/rigid-body Riemann problem, defines the force on the rigid body as a sum of the usual fluid surface forces (due to the pressure) plus an impedance weighted difference of the local fluid velocity and the velocity of the rigid body. The form of the added-mass terms are thus elucidated. The scheme was analyzed in one-dimension and shown to be well defined and stable, with a *large* time-step, even when the mass of the rigid body, m_b, goes to zero. In contrast the traditional FSI coupling algorithm has a time-step restriction that goes to zero as m_b approaches zero. Both a first-order accurate upwind scheme and a second-order accurate Law-Wendroff scheme were analyzed. Numerical computations in one-dimension confirmed the results of the theory and showed that the scheme was well behaved and accurate even when $m_b = 0$.

The added-mass scheme was then extended to multiple space dimensions. The result was an *added-mass* form of the Newton-Euler equations for rigid-body motion that included four added-mass tensors. The added-mass tensors couple the translational and angular velocities of the body and are defined in terms surface integrals involving the fluid impedance. Numerical results in two-dimensions were presented for both smooth and discontinuous problems. Second-order convergence was demonstrated using a smoothly receding piston problem with known exact solution, and a smoothly accelerated ellipse. The robustness of the scheme was demonstrated for the difficult case of a shock impacting an ellipse with zero mass and zero moment of inertia. The solution to this problem was computed on a sequence of grids of increasing resolution (utilizing adaptive mesh refinement), with the results on the different grids comparing favourably.

There are a number of avenues open for follow-on work including the extension of the current scheme to three dimensions and viscous flows. In addition, we are currently investigating approaches for coupling incompressible flow with light bodies (both rigid and deformable).

Appendix A. An analytic solution for the one-dimensional FSI model problem

Consider the problem described in figure 2. It will greatly simplify the ensuing presentation to assume the width of the rigid body is zero so that $w_b = 0$. Notice that this is only done only to simplify the presentation. Solutions for finite width are trivial to generate from the $w_b = 0$ case. Let the displacements in the left and right domains be defined by $U_L(x,t) = \int_0^t v_L(x,\tau)\,d\tau$ and $U_R(x,t) = \int_0^t v_R(x,\tau)\,d\tau$ respectively, and let the rigid body position be given by $U_b(t)$. Second-order wave equations

$$\partial_{tt}U_L(x,t) - c_L^2\partial_{xx}U_L(x,t) = 0, \quad \text{for } x < 0 \tag{A.1}$$

$$\partial_{tt}U_R(x,t) - c_R^2\partial_{xx}U_R(x,t) = 0, \quad \text{for } x > 0, \tag{A.2}$$

describe the evolution of U_L and U_R. The evolution of the rigid body position is given by the rigid body equations of motion with the applied stress determining the force on the body

$$m_b\partial_{tt}U_b(t) = \rho_R c_R^2 \partial_x U_R(0,t) - \rho_L c_L^2 \partial_x U_L(0,t). \tag{A.3}$$

Assume given initial conditions

$$U_L(x,0) = U_0(x), \qquad \partial_t U_L(x,0) = V_0(x), \quad \text{for } x < 0 \tag{A.4}$$

$$U_R(x,0) = U_0(x), \qquad \partial_t U_R(x,0) = V_0(x), \quad \text{for } x > 0 \tag{A.5}$$

$$U_b(0) = U_0(0), \qquad \partial_t U_b(0) = V_0(0). \tag{A.6}$$

The exact solution for $x < 0$ can be written in terms of the d'Alembert solution as

$$U_L(x,t) = f_L(x - c_L t) + g_L(x + c_L t) \tag{A.7}$$

where

$$f_L(\xi) = \frac{1}{2}\left(U_0(\xi) - \frac{1}{c_L}\int_0^\xi V_0(s)\,ds\right) \tag{A.8}$$

$$g_L(\xi) = \begin{cases} \frac{1}{2}\left(U_0(\xi) + \frac{1}{c_L}\int_0^\xi V_0(s)\,ds\right) & \text{for } \xi < 0 \\ U_b\left(\frac{\xi}{c_L}\right) - f_L(-\xi) & \text{else.} \end{cases} \tag{A.9}$$

Likewise for $x > 0$, the solution can be written

$$U_R(x,t) = f_R(x - c_R t) + g_R(x + c_R t) \tag{A.10}$$

where

$$f_R(\xi) = \begin{cases} \frac{1}{2}\left(U_0(\xi) - \frac{1}{c_R}\int_0^\xi V_0(s)\,ds\right) & \text{for } \xi > 0 \\ U_b\left(\frac{-\xi}{c_R}\right) - g_R(-\xi) & \text{else} \end{cases} \tag{A.11}$$

$$g_R(\xi) = \frac{1}{2}\left(U_0(\xi) + \frac{1}{c_R}\int_0^\xi V_0(s)\,ds\right). \tag{A.12}$$

For $x \leq -c_L t$ or $x \geq c_R t$ the solution given by the usual d'Alembert solution for the Cauchy problem,

$$U(x,t) = \frac{1}{2}\left(U_0(x-ct) + U_0(x+ct)\right) + \frac{1}{2c}\int_{x-ct}^{x+ct} V_0(s)\,ds,$$

where $c = c_L$ or $c = c_R$ for the left and right domains, respectively. For $-c_L t < x < c_R t$, the left and right solutions couple through the rigid body. For this case, the unknown interface position U_b is therefore found as the solution to the linear ODE

$$m_b \partial_{tt} U_b(t) + (z_R + z_L)\,\partial_t U_b(t) = g(t) \tag{A.13}$$

where $g(t) = \rho_R c_R^2 \partial_x U_0(c_R t) - \rho_L c_L^2 \partial_x U_0(-c_L t) + z_R V_0(c_R t) + z_L V_0(-c_L t)$. Solutions to the corresponding homogeneous ODE $m_b \partial_{tt}\eta(t) + (z_R + z_L)\,\partial_t \eta(t) = 0$ are easily found as

$$\eta_1(t) = e^{-t(z_R+z_L)/m_b}, \quad \text{and} \quad \eta_2(t) = 1.$$

The method of variation of parameters can be used to derive an exact solution to (A.13) as

$$U_b(t) = k_1(t)\eta_1(t) + k_2(t)\eta_2(t). \tag{A.14}$$

The unknown functions $k_1(t)$ and $k_2(t)$ are found as

$$k_1(t) = -\int \frac{\eta_1(t)g(t)}{W[\eta_1,\eta_2](t)}\,dt + \text{const} \tag{A.15}$$

$$k_2(t) = \int \frac{\eta_2(t)g(t)}{W[\eta_1,\eta_2](t)}\,dt + \text{const} \tag{A.16}$$

where $W[\eta_1,\eta_2](t)$ is the Wronskian of the homogeneous solutions. The integration constants are determined by the initial conditions. For a more detailed discussion on solution methods for (A.13) refer to [23] for example.

A specific solution of the form (A.14) is determined by specifying initial conditions $U_0(x)$ and $V_0(x)$. We illustrate with an example where an initial Gaussian pulse (of velocity and stress) moves from left to right and interacts with the rigid body and fluid domains as time progresses. Let the initial conditions be given as

$$U_0(x) = -\frac{1}{4}\frac{\sqrt{\pi}\,\text{erf}\left(\beta(x-x_0)\right)}{\beta} \tag{A.17}$$

$$V_0(x) = \frac{c_L}{2}\exp\left(-\beta^2(x-x_0)^2\right). \tag{A.18}$$

Here $\beta > 0$ and $x_0 < 0$ are parameters used to define the center and width of the initial pulse. Also notice that we envision the pulse to originate entirely in the left domain which is the reason for the appearance of c_L in the initial condition definition. The velocity of the rigid body can be found as

$$\begin{aligned}
\dot{U}_b(t) = {}& \frac{z_R(c_R - c_L)\sqrt{\pi}}{4c_R\beta m_b}\exp\left(\frac{(z_L+z_R)(z_L+z_R-4\beta^2 m_b c_R(c_R t - x_0))}{4c_R^2 m_b^2 \beta^2}\right) \\
& \left[\text{erf}\left(\frac{z_L+z_R-2c_R\beta^2 m_b(c_R t - x_0)}{2c_R m_b \beta}\right) - \text{erf}\left(\frac{z_L+z_R+2c_R\beta^2 m_b x_0}{2c_R m_b \beta}\right)\right] - \\
& \frac{z_L\sqrt{\pi}}{2\beta m_b}\exp\left(\frac{(z_L+z_R)(z_L+z_R-4c_L\beta^2 m_b(c_L t + x_0))}{4c_L^2 m_b^2 \beta^2}\right) \\
& \left[\text{erf}\left(\frac{z_L+z_R-2c_L\beta^2 m_b(c_L t + x_0)}{2c_L m_b \beta}\right) - \text{erf}\left(\frac{z_L+z_R-2c_L\beta^2 m_b x_0}{2c_L m_b \beta}\right)\right] + \\
& \frac{c_L}{2}\exp\left(-\beta^2 x_0^2 - \frac{(z_L+z_R)t}{m_b}\right).
\end{aligned} \tag{A.19}$$

Analytic expressions for the position and acceleration are determined by integration and differentiation respectively. Note that (A.19) is not easily evaluated numerically with standard math libraries as $m_b \to 0$. For the small mass case, (A.19) can be evaluated using asymptotic expansion of the error functions as their arguments approaches infinity. The desired level of accuracy can be obtained by appropriately truncation the resulting series expansion. In practice, we find that for $m_b \lesssim 0.1$ such a procedure should be used.

Appendix B. Examples of added mass matrices for constant fluid impedance

In this section we illustrate the form of the added mass matrices defined by (93)-(94), for some common body shapes when the fluid impedance is taken as constant. We denote the entries of A^{vv} by a_{ij}^{vv}, the entries of $A^{v\omega}$ by $a_{ij}^{v\omega}$ and the entries of $A^{\omega\omega}$ by $a_{ij}^{\omega\omega}$.

Appendix B.1. Added-mass matrices for an ellipse

Consider a two dimensional ellipse with semi-axes of length a and b and center of mass $\mathbf{x}_0 = \mathbf{0}$. Let the fluid impedance z_f be constant. A point on the ellipse is $\mathbf{x}(\theta) = [a\cos(\theta), \; b\sin(\theta), \; 0]^T$. The tangent to this point is $d\mathbf{x}/d\theta = [-a\sin(\theta), \; b\cos(\theta), \; 0]^T / \sqrt{a^2\sin^2(\theta) + b^2\cos^2(\theta)}$. Thus

$$\mathbf{n} = [b\cos(\theta), \; a\sin(\theta), \; 0]^T / \sqrt{a^2\sin^2(\theta) + b^2\cos^2(\theta)},$$

$$\mathbf{y} = [a\cos(\theta), \; b\sin\theta, \; 0]^T,$$

and

$$Y\mathbf{n} = [0, \; 0, \; (a^2 - b^2)\cos(\theta)\sin(\theta)]^T / \sqrt{a^2\sin^2(\theta) + b^2\cos^2(\theta)}.$$

Thus (leaving out some zero rows and columns which do not apply in two-dimensions)

$$\mathbf{n}\mathbf{n}^T = \frac{1}{a^2\sin^2(\theta) + b^2\cos^2(\theta)} \begin{bmatrix} b^2\cos^2(\theta) & ab\cos(\theta)\sin(\theta) \\ ab\cos(\theta)\sin(\theta) & a^2\sin^2(\theta) \end{bmatrix}, \tag{B.1}$$

$$Y\mathbf{n}(Y\mathbf{n})^T = \frac{1}{a^2\sin^2(\theta) + b^2\cos^2(\theta)} \begin{bmatrix} 0 & 0 & 0 \\ 0 & 0 & 0 \\ 0 & 0 & (a^2 - b^2)^2\cos^2(\theta)\sin^2(\theta) \end{bmatrix}. \tag{B.2}$$

The increment in arclength is $ds = \sqrt{d\mathbf{x}\cdot d\mathbf{x}} = \sqrt{a^2\sin^2(\theta) + b^2\cos^2(\theta)}\, d\theta$. Thus

$$A^{vv} = \begin{bmatrix} a_{11}^{vv} & a_{12}^{vv} \\ a_{21}^{vv} & a_{22}^{vv} \end{bmatrix} = \int_0^{2\pi} \frac{z_f}{\sqrt{a^2\sin^2(\theta) + b^2\cos^2(\theta)}} \begin{bmatrix} b^2\cos^2(\theta) & ab\cos(\theta)\sin(\theta) \\ ab\cos(\theta)\sin(\theta) & a^2\sin^2(\theta) \end{bmatrix} d\theta, \tag{B.3}$$

$$A^{\omega\omega} = \begin{bmatrix} 0 & 0 & 0 \\ 0 & 0 & 0 \\ 0 & 0 & a_{33}^{\omega\omega} \end{bmatrix} = \int_0^{2\pi} \frac{z_f}{\sqrt{a^2\sin^2(\theta) + b^2\cos^2(\theta)}} \begin{bmatrix} 0 & 0 & 0 \\ 0 & 0 & 0 \\ 0 & 0 & (a^2 - b^2)^2\cos^2(\theta)\sin^2(\theta) \end{bmatrix} d\theta, \tag{B.4}$$

and

$$A^{v\omega} = (A^{\omega v})^T = \begin{bmatrix} 0 & 0 & a_{13}^{v\omega} \\ 0 & 0 & a_{23}^{v\omega} \\ 0 & 0 & 0 \end{bmatrix} = \int_0^{2\pi} \frac{z_f}{\sqrt{a^2\sin^2(\theta) + b^2\cos^2(\theta)}} \begin{bmatrix} 0 & 0 & b(a^2 - b^2)\cos^2(\theta)\sin(\theta) \\ 0 & 0 & a(a^2 - b^2)\cos(\theta)\sin^2(\theta) \\ 0 & 0 & 0 \end{bmatrix} d\theta \tag{B.5}$$

Values for a_{11}^{vv}, a_{22}^{vv}, and $a_{33}^{\omega\omega}$, (which can be written in terms of elliptic integrals) for some ratios of b to a are given in Figure B.17. The values for a_{12}^{vv}, $a_{13}^{v\omega}$ and $a_{23}^{v\omega}$ are zero for uniform z_f (but can be non-zero when z_f varies). Note that for the case of a circle, $a = b$, $a_{11}^{vv} = a_{22}^{vv} = (z_f/a)\pi a^2$ where πa^2 is the area of the circle. Compare this result to that for the sphere in Section Appendix B.2.

	$b = a$	$b = a/2$	$b = a/10$	$b = a/100$
a_{11}^{vv}	$\pi z_f a$	$1.26 z_f a$	$.108 z_f a$	$.0020 z_f a$
a_{22}^{vv}	$\pi z_f a$	$3.58 z_f a$	$3.96 z_f a$	$3.99 z_f a$
$a_{33}^{\omega\omega}$	0	$.581 z_f a^3$	$1.27 z_f a^3$	$1.33 z_f a^3$

Figure B.17: Components of the added-mass matrices for an ellipse for various values of b/a with constant z_f. Values for $b/a \neq 1$ are approximate.

Appendix B.2. Added-mass matrices for an ellipsoid

We consider an ellipsoid with semi axes of length a, b and c and center of mass at $\mathbf{x}_0 = \mathbf{0}$. A point on the surface of the ellipsoid is given by

$$\mathbf{x}(\theta, \phi) = [a \sin(\phi) \cos(\theta), b \sin(\phi) \sin(\theta), c \cos(\phi)]^T, \quad \phi \in [0, \pi], \quad \theta \in [0, 2\pi].$$

From this formula it is straightforward to determine $\mathbf{n}$ and $Y\mathbf{n}$ in the formulae for the added mass matrices. For a sphere of radius a, i.e. $a = b = c$, we get ($4\pi/3 \approx 4.18879$)

$$A^{vv} = z_f a^2 \begin{bmatrix} 4\pi/3 & 0 & 0 \\ 0 & 4\pi/3 & 0 \\ 0 & 0 & 4\pi/3 \end{bmatrix}, \quad A^{v\omega} = z_f a^2 \begin{bmatrix} 0 & 0 & 0 \\ 0 & 0 & 0 \\ 0 & 0 & 0 \end{bmatrix}, \quad A^{\omega\omega} = z_f a^2 \begin{bmatrix} 0 & 0 & 0 \\ 0 & 0 & 0 \\ 0 & 0 & 0 \end{bmatrix}. \tag{B.6}$$

Recall that the volume of the sphere is $V = 4\pi a^3/3$ so that $a_{ii}^{vv} = (z_f/a)V$, $i = 1, 2, 3$. The rotational added-mass entries $a_{ii}^{\omega\omega}$, $i = 1, 2, 3$ are zero since a rotating sphere exerts no force on the adjacent (inviscid) fluid.

For $b = a$, $c = 2a$, we can compute the added-mass matrix entries approximately by quadrature giving the values

$$A^{vv} = z_f a^2 \begin{bmatrix} 9.254 & 0 & 0 \\ 0 & 9.254 & 0 \\ 0 & 0 & 2.971 \end{bmatrix}, \quad A^{v\omega} = z_f a^2 \begin{bmatrix} 0 & 0 & 0 \\ 0 & 0 & 0 \\ 0 & 0 & 0 \end{bmatrix}, \quad A^{\omega\omega} = z_f a^2 \begin{bmatrix} 4.712 & 0 & 0 \\ 0 & 4.712 & 0 \\ 0 & 0 & 0 \end{bmatrix}. \tag{B.7}$$

This ellipsoid is longest along the z-axis and has circular cross-sections for z constant. The values of a_{11}^{vv} and a_{22}^{vv} are larger than a_{33}^{vv} which indicates that the added mass is larger for translational motions in the x- or y-directions compared to the z-direction. In other words is takes more force to move the ellipsoid in the $x-$ or $y-$directions compared to the z-direction. This is consistent with the shape of the ellipsoid which is longest along the z-axis and thus has a greater effective cross-sectional area when viewed from the $x-$ or $y-$directions.

For $b = 2a$, $c = 3a$, the added-mass matrix entries are given approximately by

$$A^{vv} = z_f a^2 \begin{bmatrix} 32.307 & 0 & 0 \\ 0 & 11.023 & 0 \\ 0 & 0 & 5.552 \end{bmatrix}, \quad A^{v\omega} = z_f a^2 \begin{bmatrix} 0 & 0 & 0 \\ 0 & 0 & 0 \\ 0 & 0 & 0 \end{bmatrix}, \quad A^{\omega\omega} = z_f a^2 \begin{bmatrix} 6.840 & 0 & 0 \\ 0 & 53.511 & 0 \\ 0 & 0 & 15.963 \end{bmatrix}. \tag{B.8}$$

In this case, the translational added mass a_{11}^{vv} is largest, consistent with the effective cross-sectional area being largest when the ellipsoid is viewed in the x-direction. In other words it takes more force to move the ellipsoid in the x-direction, compared to the other directions.

Appendix B.3. Added-mass matrices for a rectangle

Consider a rectangular body of length l_x, height l_y, and center of mass $\mathbf{x} = 0$. The added-mass matrices for bodies with piecewise constant surfaces are easily computed, and we simply present the result.

$$A^{vv} = z_f \begin{bmatrix} 2l_y & 0 & 0 \\ 0 & 2l_x & 0 \\ 0 & 0 & 0 \end{bmatrix}, \quad A^{v\omega} = z_f \begin{bmatrix} 0 & 0 & 0 \\ 0 & 0 & 0 \\ 0 & 0 & 0 \end{bmatrix}, \quad A^{\omega\omega} = z_f \begin{bmatrix} 0 & 0 & 0 \\ 0 & 0 & 0 \\ 0 & 0 & \frac{1}{6}\left(l_x^3 + l_y^3\right) \end{bmatrix}. \tag{B.9}$$

Appendix B.4. Added-mass matrices for a rectangular prism

Finally, consider a rectangular prism with dimensions l_x, l_y, l_z, and center of mass $\mathbf{x} = 0$. The added-mass matrices are

$$A^{vv} = z_f \begin{bmatrix} 2l_y l_z & 0 & 0 \\ 0 & 2l_x l_z & 0 \\ 0 & 0 & 2l_x l_y \end{bmatrix}, \quad A^{v\omega} = z_f \begin{bmatrix} 0 & 0 & 0 \\ 0 & 0 & 0 \\ 0 & 0 & 0 \end{bmatrix}, \quad A^{\omega\omega} = z_f \begin{bmatrix} \frac{l_x}{6}\left(l_y^3 + l_z^3\right) & 0 & 0 \\ 0 & \frac{l_y}{6}\left(l_x^3 + l_z^3\right) & 0 \\ 0 & 0 & \frac{l_z}{6}\left(l_x^3 + l_y^3\right) \end{bmatrix}.$$
$$\tag{B.10}$$

References

[1] J. W. Banks, B. Sjögreen, A normal mode stability analysis of numerical interface conditions for fluid/structure interaction, Commun. Comput. Phys. 10 (2) (2011) 279–304.

[2] J. W. Banks, W. D. Henshaw, D. W. Schwendeman, Deforming composite grids for solving fluid structure problems, J. Comput. Phys. (to appear).

[3] B. Sjögreen, J. W. Banks, Stability of finite diference discretizations of multi-physics interface conditions, Commun. Comput. Phys. (to appear).

[4] H.-J. Bungartz, M. Schäfer (Eds.), Fluid-Structure Interaction: Modelling, Simulation, Optimization, Springer-Verlag, 2006.

[5] M. Parmar, A. Haselbacher, S. Balachandar, On the unsteady inviscid forces on cylinders and spheres in sub-critical compressible flow, Philos. T. R. Soc. Lond. A. 366 (2008) 2161–2175.

[6] B. Gustafsson, H.-O. Kreiss, A. Sundström, Stability theory of difference approximations for mixed initial boundary value problems. II, Math. Comput. 26 (119) (1972) 649–686.

[7] W. D. Henshaw, D. W. Schwendeman, Moving overlapping grids with adaptive mesh refinement for high-speed reactive and non-reactive flow, J. Comput. Phys. 216 (2) (2006) 744–779.

[8] F. Cirak, R. Deiterding, S. Mauch, Large-scale fluid-structure interaction simulation of viscoplastic and fracturing thin-shells subjected to shocks and detonations, Comput. Struct. 85 (2007) 1049–1065.

[9] I. Borazjani, L. Ge, F. Sotiropolous, Curvilinear immersed boundary method for simulating fluid structure interaction with complex 3d rigid bodies, J. Comput. Phys. 227 (2008) 7587–7620.

[10] J. Grétarsson, N. Kwatra, R. Fedkiw, Numerically stable fluid-structure interactions between compressible flow and solid structures, J. Comput. Phys. 230 (2011) 3062–3084.

[11] M. Arienti, P. Hung, E. Morano, J. E. Shepherd, A level set approach to EulerianLagrangian coupling, J. Comput. Phys. 185 (2003) 213–251.

[12] P. T. Barton, B. Obadia, D. Drikakis, A conservative level-set based method for compressible solid/fluid problems on fixed grids, J. Comput. Phys. 230 (2011) 7867–7890.

[13] R. van Loon, P. Anderson, F. N. van de Vosse, S. J. Sherwin, Comparison of various fluid-structure interaction methods for deformable bodies, Comput. Struct. 85 (2007) 833–843.

[14] J. Donea, S. Giuliani, J. P. Halluex, An arbitrary LagrangianEulerian finite element method for transient dynamic fluid-structure interactions, Comput. Method. Appl. Mech. Engrg. 33 (1982) 689–723.

[15] R. Löhner, C. Yang, J. D. Baum, H. Luo, D. Pelessone, C. M. Charman, The numerical simulation of strongly unsteady flow with hundreds of moving bodies, Int. J. Numer. Meth. Fl. 31 (1999) 113–120.

[16] E. Kuhl, S. Hulshoff, R. de Borst, An arbitray lagrangian eulerian finite-element approach for fluid-structure interaction phenomena, Int. J. Numer. Meth. Eng. 57 (2003) 117–142.

[17] H. T. Ahn, Y. Kallinderis, Strongly coupled flow/structure interactions with a geometrically conservative ALE scheme on general hybrid meshes, J. Comput. Phys. 219 (2006) 671–696.

[18] M. Schäfer, I. Teschauer, Numerical simulation of coupled fluid-solid problems, Comput. Method. Appl. Mech. Engrg. 190 (2001) 3645–3667.

[19] T. E. Tezduyar, S. Sathe, R. Keedy, K. Stein, Space-time finite element techniques for computation of fluid-structure interactions, Comput. Method. Appl. Mech. Engrg. 195 (2006) 2002–2027.

[20] R. Alexander, Diagonally implicit Runge-Kutta methods for stiff O.D.E.'s, SIAM J. Numer. Anal. 14 (6) (1977) 1006–1021.

[21] W. D. Henshaw, D. W. Schwendeman, Parallel computation of three-dimensional flows using overlapping grids with adaptive mesh refinement, J. Comput. Phys. 227 (16) (2008) 7469–7502.

[22] J. W. Banks, W. D. Henshaw, J. N. Shadid, An evaluation of the FCT method for high-speed flows on structured overlapping grids, J. Comput. Phys. 228 (15) (2009) 5349–5369.

[23] W. E. Boyce, R. C. DiPrima, Elementary Differential Equations and Boundary Value Problems (sixth edition), John Wiley & Sons, Inc., 1997.